ABSTRACT

A STATISTICAL ULTRA WIDEBAND INDOOR CHANNEL MODEL AND THE EFFECTS OF ANTENNA DIRECTIVITY ON MULTIPATH DELAY SPREAD AND PATH LOSS IN ULTRA WIDEBAND INDOOR CHANNELS

by
Jason Anthony Dabin

Ultra-wideband (UWB) indoor frequency domain channel measurements have been performed in the 2 GHz to 6 GHz frequency band using three different transmitter/receiver (Tx/Rx) antenna combination pairs. The effects of antenna directivity on path loss and multipath propagation in the channel were analyzed extensively for various omni-directional and directional antenna combinations. A statistical model of the path loss in the channel is presented, where the parameters in the model (i.e., path loss exponent and shadow fading statistics) are dependent on the particular Tx/Rx antenna combination. Time domain statistics of the channel (i.e., mean delay spread and RMS delay spread) are analyzed thoroughly for each antenna combination. Results show that RMS delay spread increases over distance for all three antenna combinations, but at a greater rate when directional antennas are used in the channel. There is a significant reduction in RMS delay spread when directional antennas are used at the transmitter and receiver or solely at the receiver with respect to an omni-directional/omni-directional antenna pair. Results show that directional antennas can be used as an effective way of mitigating the effects of multipath propagation in UWB indoor channels. A distance dependent statistical impulse response model of the channel is also presented, which statistically reproduces the impulse response of the channel with high fidelity.

A STATISTICAL ULTRA WIDEBAND INDOOR CHANNEL MODEL AND THE EFFECTS OF ANTENNA DIRECTIVITY ON MULTIPATH DELAY SPREAD AND PATH LOSS IN ULTRA WIDEBAND INDOOR CHANNELS

by
Jason Anthony Dabin

A Thesis
Submitted to the Faculty of
New Jersey Institute of Technology
in Partial Fulfillment of the Requirements for the Degree of
Master of Science in Electrical Engineering

Department of Electrical and Computer Engineering

May 2004

APPROVAL PAGE

A STATISTICAL ULTRA WIDEBAND INDOOR CHANNEL MODEL AND THE EFFECTS OF ANTENNA DIRECTIVITY ON MULTIPATH DELAY SPREAD AND PATH LOSS IN ULTRA WIDEBAND INDOOR CHANNELS

Jason Anthony Dabin

Dr. Alexander M. Haimovich, Thesis Advisor — Date
Professor of Electrical and Computer Engineering, NJIT

Dr. Haim Grebel, Thesis Co-Advisor — Date
Professor of Electrical and Computer Engineering, NJIT

Dr. Larry J. Greenstein, Committee Member — Date
Research Scientist, WINLAB, Rutgers University

BIOGRAPHICAL SKETCH

Author: Jason Anthony Dabin

Degree: Master of Science

Date: May 2004

Undergraduate and Graduate Education:

- Master of Science in Electrical Engineering,
  New Jersey Institute of Technology,
  Newark, New Jersey, 2004

- Bachelor of Science in Electrical Engineering Technology,
  New Jersey Institute of Technology,
  Newark, New Jersey, 2001

- Associate of Applied Science in Electrical Engineering Technology,
  County College of Morris
  Randolph, New Jersey, 1999

Major: Electrical Engineering

Presentations and Publications:

Jason A. Dabin, Nan Ni, Alexander M. Haimovich, Edip Niver, and Haim Grebel, "The Effects of Antenna Directivity on Path Loss and Multipath Propagation in UWB Indoor Wireless Channels," Proceedings of the 2003 IEEE Conference on Ultra Wideband Systems and Technologies, Reston, VA, pp. 305-307, November 2003.

To my parents, brother, and sister

ACKNOWLEDGMENT

I sincerely express my gratitude and appreciation to Dr. Alexander M. Haimovich and Dr. Haim Grebel for all their encouragement, guidance, and support, which led to the completion of this thesis. Also, I especially thank Dr. Edip Niver for all his help and insight regarding RF measurements and channel measurement apparatus. I would like to gratefully thank Dr. Larry J. Greenstein for his many helpful insights and suggestions, and participation as a member of my committee. My appreciation and thankfulness is expressed to Dr. Saeed S. Ghassemzadeh for his many helpful suggestions.

I would like to thank Ivan Seskar of the Wireless Information Network Laboratory (WINLAB) at Rutgers University for all his assistance and helpul suggestions regarding RF measurements. Also, I would like to thank Andrej Domazetovic for his helpful discussions during his time at WINLAB as a graduate student.

Much appreciation is extended to my fellow graduate students in the Communications and Signal Processing Research Laboratory at NJIT, in particular; Nikolaus H. Lehmann, Dr. Jingdi Zeng, Nan Ni, and Hongsan Sheng for all their invaluable suggestions and support. Also, I would like to sincerely thank Marlene Toeroek for all her administrative assistance.

TABLE OF CONTENTS

TABLE OF CONTENTS
(Continued)

Chapter **Page**

LIST OF TABLES

LIST OF FIGURES

LIST OF FIGURES
(Continued)

Figure **Page**

CHAPTER 1

INTRODUCTION

An ultra-wideband (UWB) device defined by the Federal Communications Commission (FCC) must have a -10 dB fractional bandwidth greater than or equal to 20% of the center frequency or have a minimum bandwidth of 500 MHz [1]. UWB technology is being considered as a short-range (up to 10 m) wireless air interface for high speed data transmission (e.g. Wireless Personal Area Network (WPAN) IEEE standard 802.15.3a). This standard is proposed to support data rates in excess of 110 Mbps, lending itself applicable to wireless in-home networking. These data rates are unachievable in conventional wireless systems due to data rate limitations of the channel.

The wireless channel is a limiting factor in the performance of wireless systems. By knowing the characteristics of the channel, optimum methods can be developed to mitigate the effects that hinder the performance of the system. For frequency selective channels the signal bandwidth is greater then the channel coherence bandwidth, which results in multiple replicas of the transmitted signal, which are attenuated, phase shifted, and delayed in time. Furthermore, the delay spread of the channel is larger than the reciprocal bandwidth of the signal, which can greatly impede the performance of the system (i.e., data rates).

For wideband systems, it is well known that multipath delay spread in the wireless channel limits data rates due to transmission errors caused by intersymbol interference (ISI). One method to mitigate the effects of multipath propagation is to use directional antennas. The radiation or beam pattern of a directional antenna can be thought of as a

sector of an omni-directional antenna pattern. Therefore, it is less susceptible to multipath in the channel since it accepts only multipath signals that arrive within the beam pattern of the antenna. Moreover, the directional antenna limits the amount of multipath received in the channel resulting in less delay spread and the ability to achieve higher data rates. Other techniques can be developed to mitigate the impairments of frequency selective channels, but a detailed characterization of the channel is needed to guarantee optimum performance.

Wideband measurements of the indoor radio propagation channel have been studied thoroughly in [2]-[11], but are only valid for wideband channels and do not consider UWB indoor signal propagation. To understand the UWB propagation channel (i.e., path loss and multipath characteristics), field measurements must be performed and analyzed thoroughly. UWB channels have been studied using time domain and frequency domain channel sounding techniques in office and residential environments [12]-[28].

In Ghassemzadeh et al. [12][13], a characterization of the indoor UWB channel is thoroughly described for line of sight (LOS) and non-line of sight (NLOS) scenarios in residential environments. Frequency domain channel measurements were performed over the 4.375 GHz to 5.625 GHz frequency band using a Vector Network Analyzer (VNA). Measurements were performed in a total of 23 homes, resulting in over 300,000 measurements of the channel. In general, the power delay profile of the channel was shown to exhibit a single cluster arrival taking on the form of a decaying exponential, times a noise-like process with lognormal statistics. The path loss exponents and RMS delay spread values were Guassian distributed over all homes. The mean path loss values

obtained for LOS and NLOS channels were 1.7 and 3.5, respectively. The mean RMS delay spread values were 4.7 ns and 8.2 ns for LOS and NLOS, respectively.

In [14]-[17], time domain measurements of the indoor UWB channel were performed in an office environment using baseband pulses with a corresponding 2 ns delay resolution. Measurements were taken in 14 different rooms and hallways resulting in a total of 741 measurements. A statistical characterization of the channel is thoroughly described in Cassioli et al. [17]. The PDP was shown to take on the form of a decaying exponential, similar to what was observed in Ghassemzadeh [13], but without the multiplicative lognormal process.

In Kunisch [21], indoor UWB frequency domain measurements were performed in an office environment for a 1 GHz to 11 GHz frequency range. Measurements consisted of LOS, NLOS, intra-office, and inter-office scenarios. The PDP resulted in multiple decaying exponential clusters as opposed to a single cluster arrival as described in the measurements above.

The IEEE 802.15.3a task group has proposed a UWB channel model as a result of numerous channel modeling campaigns [18]. Overall, several channel modeling proposals observed a multipath clustering phenomenom, which led to a channel model based on the Saleh-Valenzuela model [11] with slight modifications.

However, these measurements do not include the effects of antenna directivity on the channel. Moreover, LOS measurements in classrooms and laboratories were not carried out extensively. This thesis examines the effects of antenna directivity on path loss and multipath propagation in a college campus building at the New Jersey Institute

of Technology (NJIT), resulting in a thorough characterization of the UWB indoor wireless channel.

In this thesis, Chapter 2 describes the measurement system, environment, and procedure. Chapter 3 describes the data reduction of the measured data for suitable representation and analysis of the path loss in the channel. From this a statistical model of the path loss is presented for different omni-directional and directional antenna combinations. Chapter 4 thoroughly analyzes the multipath characteristics of the channel through extensive analysis of the RMS delay spread of the measured impulse responses. Chapter 5 analyzes the impulse response measurements of the channel in depth and describes a statistical channel impulse response model representative of the measured data. Lastly, Chapter 6 concludes the work of this thesis.

CHAPTER 2

MEASUREMENT SYSTEM AND PROCEDURE

In this chapter, the channel sounding technique, measurement system, environment, and measurement procedure are described.

2.1 Measurement System

Frequency response measurements of the indoor UWB channel were performed using a frequency domain channel sounder shown in Figure 2.1. The channel was swept from 2 GHz to 6 GHz in intervals of 5 MHz, at a rate of 2.5 Hz. The frequency response of the channel was measured using a Hewlett Packard 8510C Vector Network Analyzer (VNA), shown in Figure 2.2. The VNA measures the magnitude and phase of each frequency component and; therefore, the inverse discrete Fourier transform (IDFT) can be used to convert the frequency domain channel response into the time domain channel response for analysis in the temporal domain. Given a frequency spacing equal to 5 MHz, the time domain window can detect a multipath component arrival up to 200 ns. This is a reasonable window length given that multipath arrivals have not been detected beyond 160 ns for a transmitter/receiver (Tx/Rx) separation distance up to 10 m [22]. A power amplifier (PA) with a maximum output of 30 dBm was used to amplify each frequency component generated by the VNA prior to propagation via the transmitting antenna. The signal from the receiving antenna was propagated through a 20 m double shielded coaxial cable with an average 17 dB loss over the corresponding measured frequency band before being returned to the VNA. Double shielded cable was used for all front end and back end connections throughout the system.

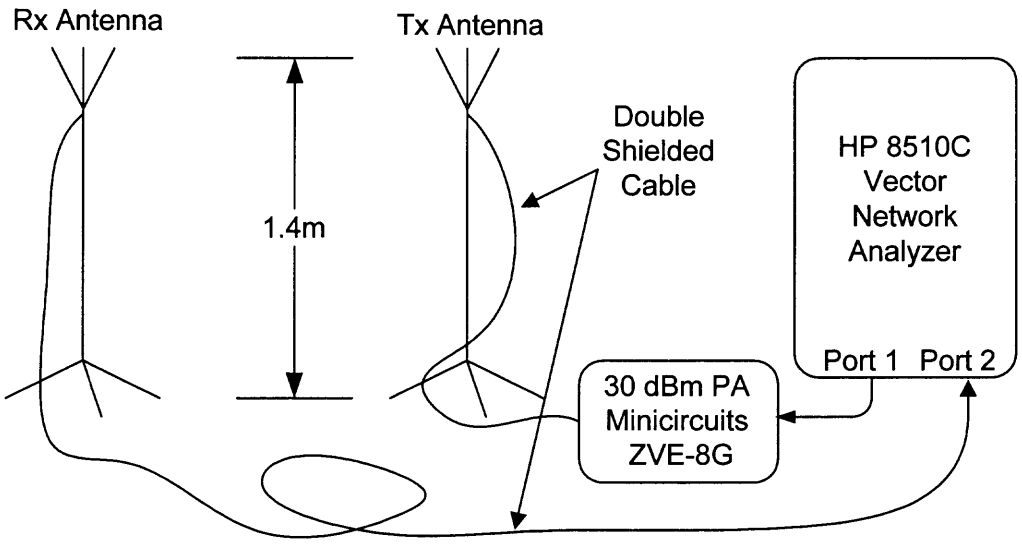

Figure 2.1. Frequency Domain Channel Sounder Measurement System.

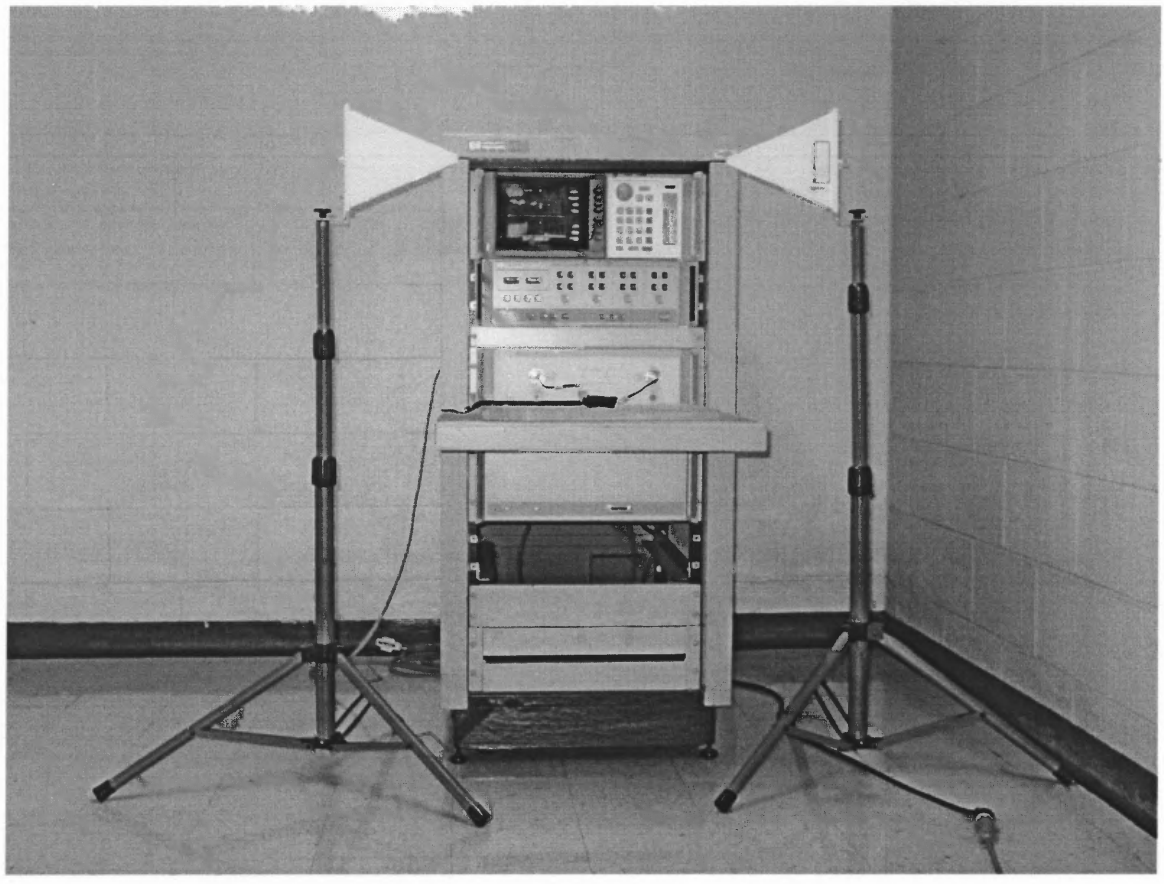

Figure 2.2. Hewlett Packard 8510C Vector Network Analyzer (VNA) (center).

Three Tx/Rx vertically polarized antenna combinations were tested using omni-directional and directional antennas. The omni-directional antenna is a linearly polarized conical monopole antenna which is omni-directional in the azimuth plane with a typical gain of 0 dBi. The directional antenna is a linearly polarized log periodic antenna with a half power beamwidth equal to 65° in the E-plane and 100° in the H-plane and has an approximate gain of 5.6 dBi.

2.2 Procedure and Environment

Measurements were performed in a classroom, an electrical engineering (EE) laboratory, and an optical science laboratory, which are all located on the fourth floor of the Faculty Hall building at NJIT. Faculty Hall is a four-story building, which mostly consists of classrooms and engineering laboratories. The floors of each measured room are made up of ceramic tiles. The classroom contains approximately forty desks surrounded by three cinder block walls and one sidewall with cinder blocks and windows with metal framing. The electrical engineering lab contains wooden lab workstations with computer terminals and various test and measurement equipment surrounded by four cinder block walls. The two sidewalls are aligned with wooden cabinets with glass windows. The optical science lab contains optical lab worktables, computer terminals on carts, metal air ducts that hang from the ceiling which are part of the air conditioning system, student desks, metal cabinets, and various other clutter surrounded by four cinder block walls.

All measurements were made while the transmitter and receiver antennas remained stationary and within line-of-sight of each other. Also, the channel was kept stationary during measurements by ensuring there was no movement in the surrounding environment. Three different Tx/Rx antenna combinations were set up to explore the effects of antenna directivity on the channel. The three Tx/Rx antenna combinations tested were omni-directional/omni-directional, directional/directional, and omni-directional/directional. Measurements were made between 1 m and 10 m in intervals of 1 m, with the exception of the classroom where measurements extended up to a maximum of 9 m. Thirty locations were measured in the EE lab, twenty in the classroom, and thirty in the optics lab for all three antenna combinations, with the

exception of the omni-directional/directional case in the optics lab in which twenty locations were measured. Therefore, a total of seventy-eight locations were measured for each antenna combination with the exception of the omni-directional/directional case in which sixty-eight locations were measured. Ten snapshots of the channel frequency response were recorded per receiver location for post-processing averaging to obtain a more stable response of the channel. The VNA was calibrated with respect to a 1 m reference distance inside an anechoic chamber for each antenna combination so that all measurements depend solely on the response of the channel. A back-to-back calibration (i.e., system calibration excluding the Tx/Rx antennas) was also carried out to assess the path loss in the channel at 1 m including the antennas as well. The measured path loss at 1 m in the anechoic chamber and the pathloss computed by averaging over the same number of frequencies using the Friis free space Equation in (2.1) resulted in a difference of at most 0.13 dB for all three antenna combinations. Therefore, a Tx/Rx separation distance of 1 m in the anechoic chamber was considered an adequate free space reference distance. The free space path loss is given by,

$$PL_{FS}(d) = \frac{G_{tx} G_{rx} \lambda^2}{(4\pi)^2 d^2}, \tag{2.1}$$

where $PL_{FS}(d)$ denotes the free space path loss, λ is the wavelength in meters, d is the distance in meters, and G_{tx} and G_{rx} denote the transmitter and receiver antenna gains, respectively. The Tx/Rx antennas were each set to a height of 1.4 m for all measurements.

2.3 Summary

This chapter described a measurement campaign for the UWB indoor channel. A description of the measurement system, procedure, and environment in which measurements were performed were thoroughly explained.

CHAPTER 3

LARGE SCALE FADING

The measured data must be processed and represented in proper form for analysis purposes. In this chapter, the data processing and representation of path loss are described. A path loss model is proposed for each antenna combination and the shadow fading in the channel is analyzed.

3.1 Data Reduction

The path loss of the channel represents the attenuation a signal undergoes when transmitted through the medium, which is represented as a positive quantity in dB. As mentioned in Chapter 2, the VNA was used to measure the frequency response of the channel, and is known to be a tractable measurement apparatus for calibrating out the effects of unwanted components for any particular system setup. This lends itself particularly useful for characterizing the path loss and multipath characteristics of the channel, where the effects of the system components must be factored out to assess the propagation channel characteristics. The path loss is given by the difference between the transmitted and received power in dB including antenna gains as well for analysis and modeling purposes. The measured frequency response was referenced to a system calibration at a distance of 1 m in an anechoic chamber as described in the measurement procedure. The squared magnitude response is given by the received power at a distance d relative to the received power at 1 m in the anechoic chamber (i.e., negative path loss in

dB). Therefore, additional processing of the data is needed for proper representation of the path loss as defined above (i.e., path loss including antenna gains and the loss at 1 m).

The average path loss of the channel at a distance d denoted by $PL(d)$ is given by the inverse of $PL'(d)$ (where $PL'(d)$ is negative in dB, which results in a positive value for $PL(d)$ in dB). The measured frequency response referenced to a distance of 1 m has a corresponding inverse path loss $PL'(d;d_0)$ given by,

$$PL'(d;d_0) = \frac{1}{NK}\sum_{i=1}^{N}\sum_{j=1}^{K}\left|H_j(f_i;d)\right|^2, \tag{3.1}$$

where $H_j(f;d)$ is the frequency response of the channel for a given snapshot j, which represents the received power relative to the transmitted power per frequency component or, rather, the attenuation in the channel over the 2 GHz to 6 GHz frequency range. N represents the number of frequency components f measured in the channel, K represents the number of snapshots, and d is the separation distance between the Tx/Rx antennas in meters.

The frequency response obtained from the VNA can be written as a ratio of the received power per frequency component at a distance d relative to the corresponding powers at a distance $d_0 = 1$ m. Therefore, the path loss obtained from the VNA averaged over the bandwidth is represented by,

$$PL'(d;d_0) = \overline{\left(\frac{P_r(f;d)/P_t}{P_{ref}(f;d_0)/P_t}\right)} = \overline{\left(\frac{P_r(f;d)}{P_{ref}(f;d_0)}\right)}, \tag{3.2}$$

where P_t is the transmitted power from the VNA, $P_r(f;d)$ is the power received by the VNA for a distance d per frequency component f and $P_{ref}(f;d_0)$ is the power received by

the VNA at a distance of 1 m in the anechoic chamber per frequency component f. The received power $P_r(f;d)$ is given by,

$$P_r(f;d) = \frac{P_t G_{tx} G_{rx} G_{PA}}{L_{cab}(f) L_{ch}(f;d)}, \tag{3.3}$$

where G_{PA} is the gain of the power amplifier, $L_{cab}(f)$ is the cable loss per frequency f, $L_{ch}(f;d)$ is the loss due to the channel corresponding to the aforementioned parameters f and d, and G_{tx} and G_{rx} are the transmitter and receiver antenna gains, respectively. Now inserting equation (3.3) into (3.2) for $P_r(f;d)$ and $P_{ref}(f;d_0) = P_r(f;d_0)$ results in,

$$PL'(d;d_0) = \overline{\left(\frac{L_{ch}(f;d_0)}{L_{ch}(f;d)} \right)}. \tag{3.4}$$

Therefore, the inverse path loss computed from the measured data is referenced to the inverse path loss at 1 m.

To assess the path loss in the channel at the close in reference distance (d_0 = 1 m), the path loss in the channel must be referenced to a back to back calibration. As mentioned previously, a back to back calibration refers to a system calibration excluding the antennas and thus can be thought of as a closed loop calibration of the entire system up to the back ends of the antennas. Therefore, all calibration data must be removed from the measured frequency response obtained from the VNA except for the back to back calibration data. Let $PL'_{ref}(f;BB)$ in Equation (3.5) denote the inverse path loss at d_0 referenced to a back to back calibration in the anechoic chamber per frequency f which is given by,

$$PL'_{ref}(f;BB) = \frac{P_{ref}(f;d_0)}{P_{cal}(f;BB)}, \tag{3.5}$$

where $P_{cal}(f;BB)$ represents the received power excluding the Tx/Rx antenna gains and the path loss of the channel and is given by,

$$P_{cal}(f;BB) = \frac{P_t G_{PA}}{L_{cab}(f)}. \tag{3.6}$$

By multiplying Equations (3.2) and (3.5) the received power $P_{ref}(f;d_0)$ in Equation (3.2) is removed and replaced with $P_{cal}(f;BB)$ the received power from the back to back calibration. Therefore, the inverse path loss in the channel is referenced to the front end and back end of the measurement system up to the antennas and is given by:

$$PL'(d) = \overline{\left(\frac{P_r(f;d)}{P_{cal}(f;BB)}\right)} = G_{tx}G_{rx} \cdot \left(\overline{L_{ch}(f;d)}\right)^{-1}. \tag{3.7}$$

This enables analysis of the path loss at 1 m to be assessed including antenna gains, where the path loss $PL(d)$ is given by $\left(PL'(d)\right)^{-1}$.

3.2 Path Loss Model

It is well known that the median path loss referenced to a distance d_0 can be modeled as a function of distance using the following power law relationship,

$$PL_{med}(d;d_0) \propto \left(\frac{d}{d_0}\right)^{\alpha}, \tag{3.8}$$

where α is the path loss exponent [11][12][29].

By logarithmically transforming Equation (3.8) and including the path loss at d_0, the mean path loss in dB can be modeled linearly as a function of the logarithmic distance. The mean path loss model does not account for the clutter present in the environment at different locations with the same Tx/Rx separation distance. As the

clutter in the environment changes from location to location, so does the received power, which introduces a random change in the path loss. This random variation has been shown to be log-normally distributed (Gaussian in dB with zero mean) [12][16][17][18], and is known as log-normal shadowing. Therefore, the path loss in the channel is normally distributed in dB with a mean that linearly changes with distance and is modeled as,

$$PL_{dB}(d) = \overline{PL_{dB}}(d_0) + 10 \cdot \alpha \log\left(\frac{d}{d_0}\right) + X, \tag{3.9}$$

where $\overline{PL_{dB}}(d_0)$ denotes the mean path loss at 1 m, $10 \cdot \alpha \log(d/d_0)$ denotes the mean path loss referenced to 1 m, and X is a zero mean log-normal random variable in dB. The mean path loss at d_0 and the path loss exponent α (or rather the slope of the mean of Equation (3.9)) were determined through regression analysis using the method of least squares. That is, the path loss at d_0 and the slope α were taken as estimates for which the sum of the squares of the errors between the straight line and the measured data is a minimum. The difference between the least squares fit and the measured data is represented by the log-normal random variable X. All data was pooled together globally for computing the least squares fit to the data for each antenna combination. Therefore, the measured data from all rooms was used to calculate the model parameters of Equation (3.9). A scatter plot of the path loss vs. distance along with the least squares fit to the data is shown in Figure 3.1 for each antenna combination, where the path loss is represented as a positive quantity. Normal probability plots of the deviation between the fitted and measured data (also known as residuals) for each antenna combination are shown in Figure 3.2.

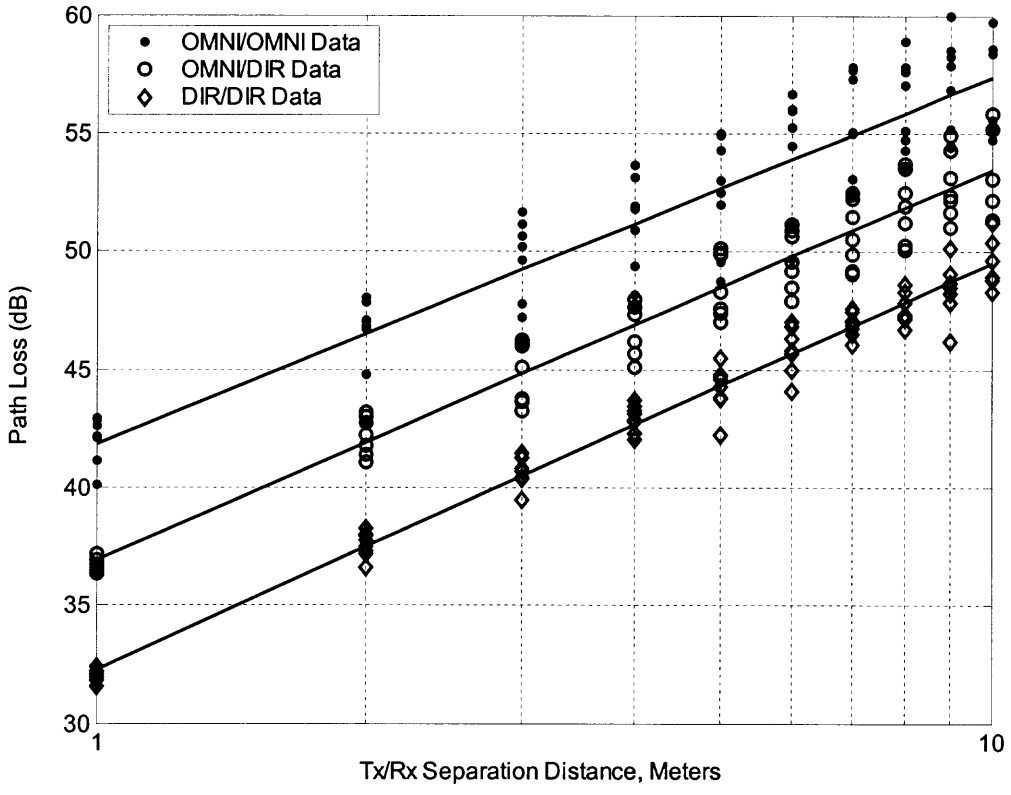

Figure 3.1. Scatter plot of path loss vs. Tx/Rx separation distance and the least squares fit to the data for all three antenna combinations.

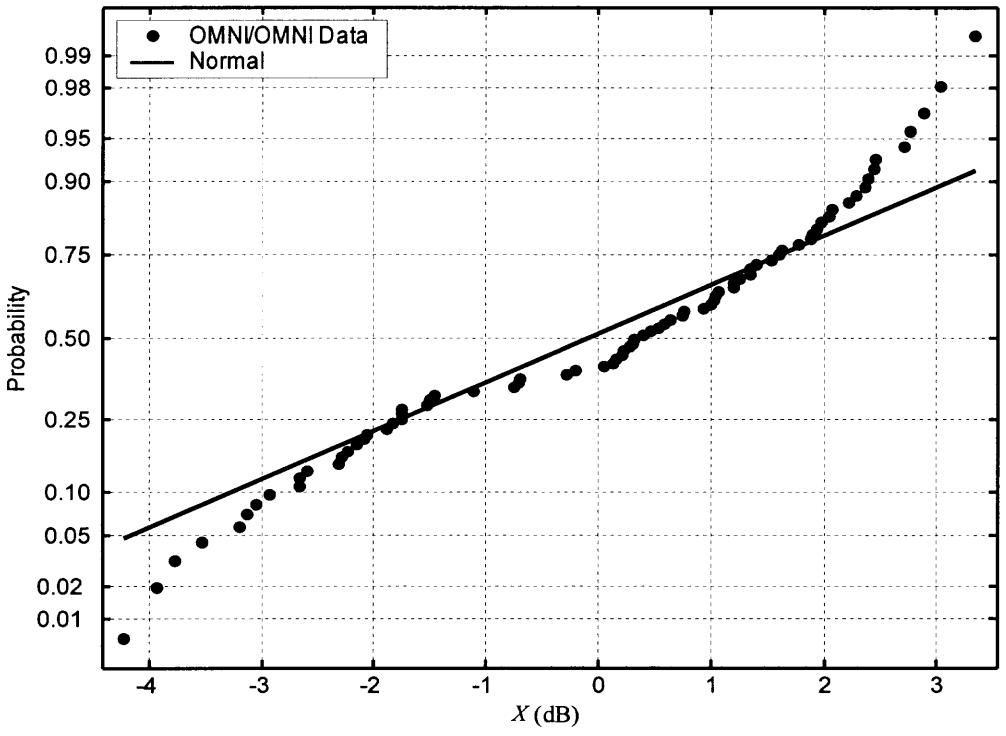

(a)

Figure 3.2. Normal probability plots of the shadow fading parameter X. (a) omni-directional/omni-directional. (b) omni-directional/directional. (c) directional/directional.

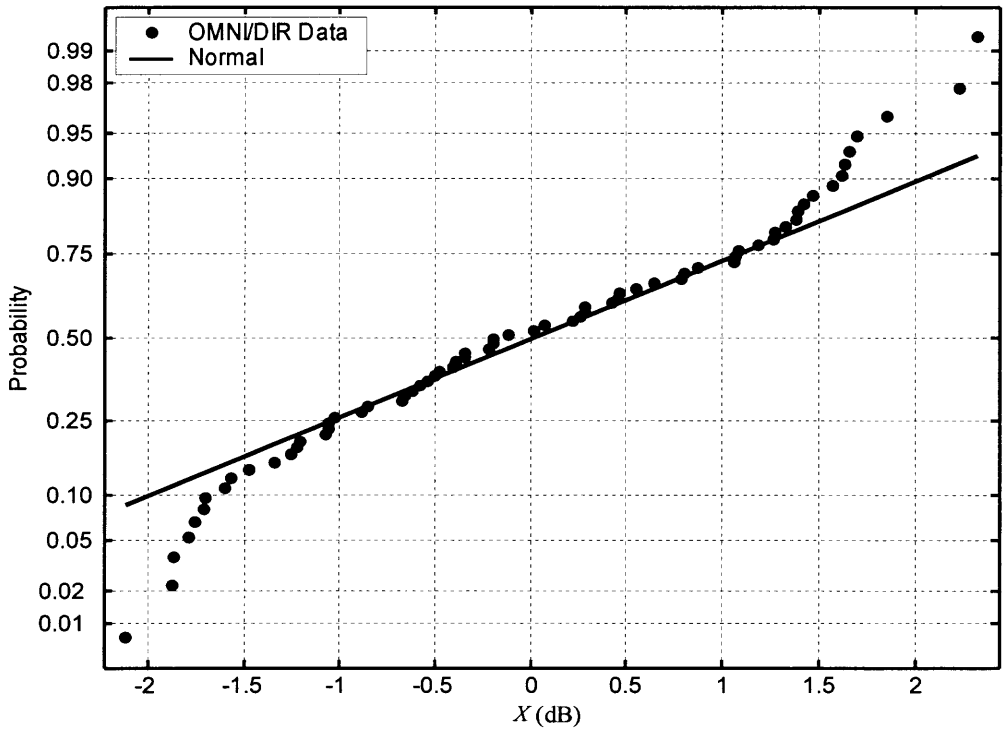

(b)

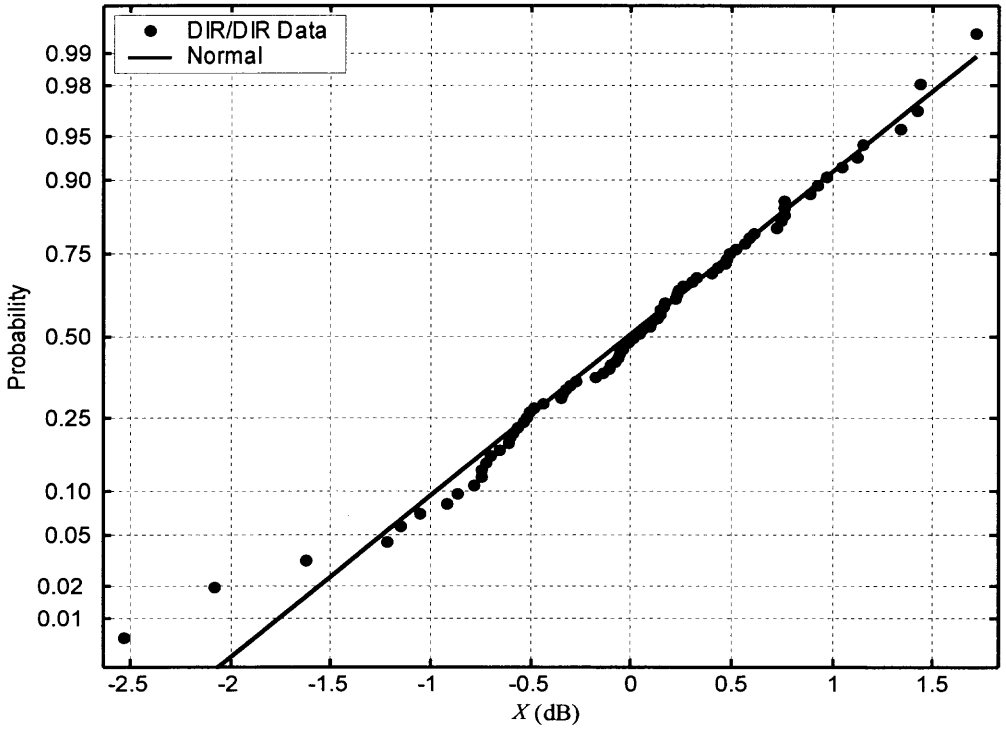

(c)

Figure 3.2. (*Continued*)

As shown in Figure 3.1, the path loss values for the dir/dir antenna combination are highly concentrated about the regression line with large deviations occurring sparsely. These values significantly agree with the normality assumption as shown in Figure 3.2c. On the other hand, the omni/omni data is sparsely distributed about the regression line and does not demonstrate a large concentration of path loss values about the least squares fit as in the dir/dir case. This is due to the sensitivity of the omni-directional antennas to homogeneous environments with differing clutter, and is illustrated in the normal probability plot of Figure 3.2a. Therefore, the clutter has a significant effect on the total received energy when using omni-directional antennas, even though the environmental characteristics of the rooms are homogeneously related. It can be deduced from the shadow fading experienced in the channel that the environment has less of an impact on the channel for an omni/dir antenna combination, than for an omni/omni antenna configuration, as shown in Figure 3.2. What's more, since a directional antenna is employed at the receiver, the channel is less vulnerable to multipath propagation experienced in different rooms due to its spatial filtering capability, which is described in Chapter 5. Therefore, in indoor environments spatial filtering provides significant multipath resistance, resulting in a more stable average path loss value for homogeneous environments with differing clutter as shown in Figures 3.1 and 3.2.

It is apparent that omni-directional antennas are more susceptible to changing environments then directional antennas, resulting in larger deviations in path loss. This can be explained from the fact that omni-directional antennas are more prone to the effects of multipath propagation than directional antennas. Therefore, when modeling the data globally, directional antennas provide a more stable model of the path loss

experienced in the environment. One way to improve the stability of modeling omni-directional data is to include more measured data in the global database to account for the large deviations of path loss experienced in the channel. Therefore, large data sets are needed to account for the dependence or impact the environment has on the channel when omni-directional antennas are employed. Another way to model the path loss in the channel is to estimate the path loss model parameters for each individual location (e.g., room) and then model the variation of these estimates over all locations [12]. It can be concluded that multipath propagation experienced in different environments (with homogeneous characteristics) has less of an effect on the path loss in the channel when directional antennas are used.

As previously mentioned, the path loss of the channel is affected by the amount of energy the antenna receives, which is a function of the antenna directivity or rather the radiation pattern of the antenna. From a radiation pattern perspective, it is evident that more multipath components are coupled from the propagation medium by an omni-directional receiving antenna as opposed to a directional receiving antenna. This can be justified through the path loss exponent, which is related to the degradation of the path loss over distance relative to 1 m. The path loss exponent for the omni/omni case is equal to 1.55 and is equal to 1.65 for the omni/dir case. The former path loss exponent is less than the latter due to the fact that an omni-directional receiving antenna collects many more multipath components in comparison to a directional receiving antenna. The path loss exponent α is 1.72 for the dir/dir case, which is greater than for either of the other two antenna combinations. This is expected, since the directional transmitter antenna limits the radiated energy to a narrow cone, resulting in fewer multipath components at

the receiver. Note that all path loss exponents are less than the corresponding free space value (α=2) due to the accumulation of considerable multipath energy as opposed to a single LOS ray, which was also observed in [9][11][12]. Table 3.1 lists the values obtained for the path loss exponent α and the standard deviation σ_{dB} of the shadow fading random variable X for each antenna combination.

Table 3.1. Path Loss Exponent α and Standard Deviation of the Shadow Fading Random Variable X

Antenna Combination	α	σ_{dB}
OMNI/OMNI	1.55	1.98
OMNI/DIR	1.65	1.19
DIR/DIR	1.72	0.77

It has been validated that the path loss at 1 m can be modeled by averaging the path loss at 1 m over the specified frequency band using the Friis free space equation. The average path loss computed in the environment at 1 m over all locations for each antenna combination resulted in a difference of at most approximately 1 dB in comparison to the corresponding free space path loss result. For example, the average path loss at 1 m over all locations for an omni/omni Tx/Rx antenna combination is 42.10 dB, and is equal to 43.23 dB using the Friis free space equation and averaging over the same frequency range. When using an omni/dir antenna combination the average measured path loss at 1 m is 36.8 dB and is theoretically equal to 37.63 dB. Furthermore, for a dir/dir antenna combination the empirical average path loss value is 32 dB, which is almost identical to the theoretical free space value of 32.03 dB. Therefore, Equation (2.1)

can be used for computing the average path loss at a distance of 1 m for the path loss model in Equation (3.9) by averaging over the specified frequency band and including the Tx/Rx antenna gains. The path loss in the channel can be predicted as a function of distance for all three antenna combinations by using Equation (3.9) along with the values in Table 3.1 and Equation (2.1), as explained previously.

3.3 Summary

In this chapter, data processing of the measured data was explained for path loss representation and analysis. A path loss model representative of all three antenna combinations was thoroughly described. Results show that path loss increases at a greater rate when directional antennas are used in the channel as opposed to omni-directional antennas. Also, the shadow fading in the environment was shown to be largest for the omni/omni antenna pair and lowest for the dir/dir antenna pair. All path loss exponents were estimated to be less than the free space value. Lastly, it was shown that the path loss at 1 m can be approximated using the Friis free space equation.

CHAPTER 4

TIME DOMAIN ANALYSIS

4.1 Data Reduction

The impulse response of the channel was obtained by performing the IDFT on the frequency response of the channel. Before performing the IDFT, the frequency domain data was first filtered using a Kaiser window with parameter $\beta = 4.54$ [30]. The non-windowed frequency spectrum can be thought of as a rectangular windowed response with frequency selectivity. Therefore, the time domain response is represented by multiple sinc functions which are attenuated and delayed in time. Using the window filtering function prior to performing the IDFT helps reduce the side lobes, which are inherent to the sinc pulses appearing or rather existing in the impulse response of the channel. This filtering procedure reduced the side lobes of the impulse response by 50 dB and broadened the main lobe width such that the time resolution has changed from 0.25 ns to 0.4 ns. The window parameter β was chosen to lower the sidelobes down to the noise floor and avoid significant effects of pulse broadening simultaneously. The time resolution derived from the non-windowed frequency response is given by the reciprocal of the bandwidth (e.g., 1/(4 GHz)). This results in a 0.5 ns null-to-null pulse width. After performing the IDFT on the windowed frequency response the main lobe of the pulse increases to approximately 0.8 ns. Note that a 4096 point zero-padded frequency response was constructed before performing the IFFT. This resulted in a sampling period T_s given by,

$$T_s = \frac{1}{(\text{total bins}) \cdot \Delta f} = \frac{1}{(4095 \cdot 5\text{MHz})} \cong .0488\,\text{ns} \tag{4.1}$$

The time axis was quantized into bins to obtain a power delay profile (PDP) in which each multipath component is represented as an impulse function weighted by the integration of the power within each bin having a width $\Delta\tau$. The bin width was chosen to correspond roughly with the aforementioned pulse width, equal to approximately 0.8 ns. Therefore, $\Delta\tau$ is chosen to be,

$$\Delta\tau = 20 \cdot T_s = .9768\,\text{ns} \tag{4.2}$$

which corresponds to a bin size slightly greater than the pulse width. Each impulse response was represented with the first arrival starting at time 0 ns. Therefore, any multipath signal arriving within the i^{th} bin is represented with a delay $\tau_i = i\Delta\tau$, for $i = 0$ to N-1, where N is the total number of possible multipath components including the first arrival [29]. The discretized impulse response of the channel is given by,

$$h(\tau;d) = \sum_{i=0}^{N-1} a_i(\tau;d) e^{j\theta_i(\tau;d)} \delta(\tau - \tau_i), \tag{4.3}$$

where d represents the Tx/Rx separation distance, a_i denotes the amplitude of the i^{th} multipath component, θ_i denotes the phase associated with the i^{th} multipath component, and δ is the Dirac delta function.

The PDP of the channel is characterized by averaging many snapshots of $|h(\tau;d)|^2$ over a spatial local area. For wideband signals, it is known that multipath fading statistics of the channel do not change significantly over a local area [6][8]. Therefore, wideband channels are considered wide-sense stationary over small spatial distances; which concludes that multipath statistics at a single location are representative of the multipath statistics in the corresponding local area. Given the ultra-wide bandwidth of the measured frequency response (see Chapter 2) it can be concluded, that averaging the

PDP over K snapshots in a single location approximates the spatial average of the PDP with high accuracy. Therefore, the PDP of the channel is given by:

$$P(\tau;d)=\frac{1}{K}\sum_{k=1}^{K}\left|h_k(\tau;d)\right|^2=\sum_{i=0}^{N-1}\left|h(\tau_i;d)\right|^2\delta(\tau-\tau_i)=\sum_{i=0}^{N-1}\left|a_i(\tau;d)\right|^2\delta(\tau-\tau_i), \quad (4.4)$$

where K represents the number of snapshots of the channel $h_k(\tau;d)$ taken at a single location, and $\left|h(\tau;d)\right|^2$ represents the average PDP.

The noise floor was removed from the PDP prior to time quantization to eliminate noise spikes appearing as false multipath components [31]. The noise threshold was set 2 dB above the maximum noise component detected prior to the first multipath component arrival (e.g., LOS Signal). All power below this threshold was set to zero, resulting in a PDP with 98.3% energy capture after noise reduction on the average.

4.2 Multipath Delay Spread Analysis

The multipath in the channel is most commonly characterized quantitatively by the first moment and the square root of the second central moment of the PDP, referred to as the mean delay spread and the root mean square (RMS) delay spread, respectively. The RMS delay spread can be used as a figure of merit for estimating data rates for multipath channels [29]. The RMS delay spread σ_τ is defined as,

$$\sigma_\tau=\sqrt{\frac{\sum_{i=0}^{N-1}(\tau_i-\tau_m)^2\left|a_i\right|^2}{\sum_{i=0}^{N-1}\left|a_i\right|^2}}. \quad (4.5)$$

where the mean delay spread τ_m is defined as,

$$\tau_m = \frac{\sum_{i=0}^{N-1} \tau_i \cdot |a_i|^2}{\sum_{i=0}^{N-1} |a_i|^2}. \tag{4.6}$$

Figure 4.1 shows the cumulative distribution function (CDF) of σ_τ for each antenna combination. Tables 4.1 and 4.2 list the mean, minimum, median, and maximum values of σ_τ and τ_m, respectively. It is evident from Figure 4.1 and Table 4.1 that the RMS delay spread decreases when directional antennas are introduced into the channel, or rather when the beamwidth of the antenna decreases.

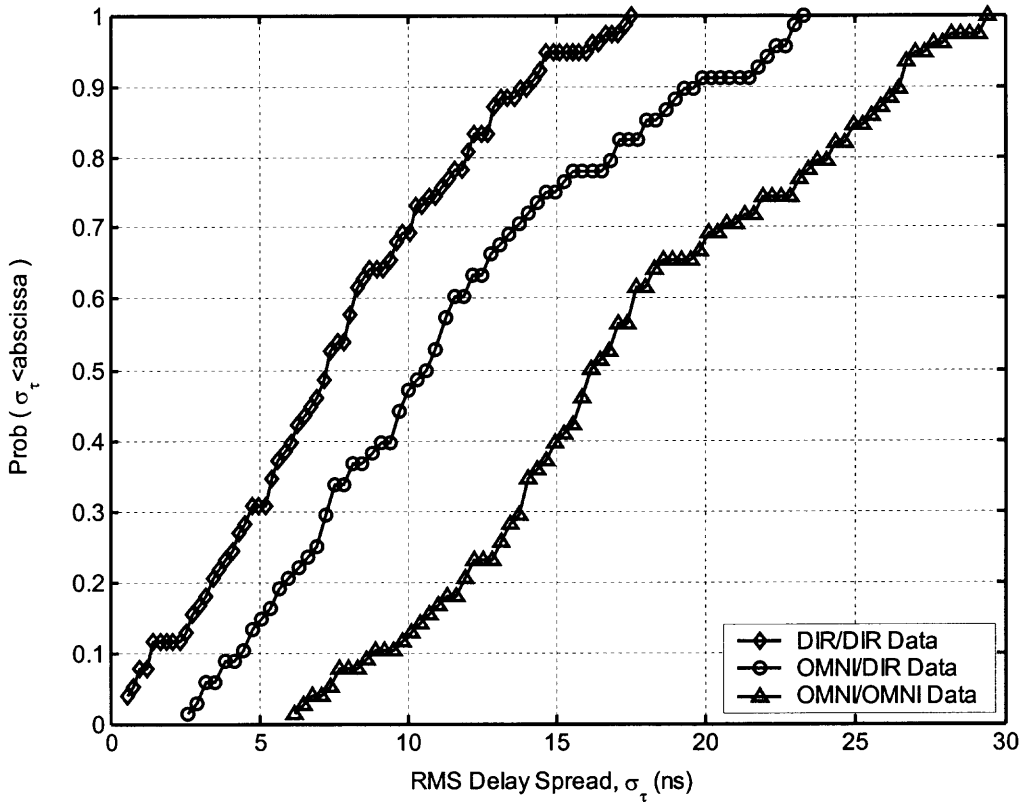

Figure 4.1. CDF of RMS delay spread values over all locations for each antenna combination.

Table 4.1. Descriptive Statistics of RMS Delay Spread for All Three Antenna Combinations

Antenna Combination	$\bar{\sigma}_\tau$ (ns)	min σ_τ (ns)	med σ_τ (ns)	max σ_τ (ns)
OMNI/OMNI	17.34	6.05	16.41	29.60
OMNI/DIR	11.35	2.44	10.80	23.45
DIR/DIR	7.71	0.46	7.35	17.64

Table 4.2. Descriptive Statistics of the Mean Delay Spread for All Three Antenna Combinations

Antenna Combination	$\bar{\tau}_m$ (ns)	min τ_m (ns)	med τ_m (ns)	max τ_m (ns)
OMNI/OMNI	11.86	3.68	10.42	30.90
OMNI/DIR	5.59	0.38	4.59	16.75
DIR/DIR	2.04	0.03	1.70	7.46

The minimum RMS delay spread for the omni/dir case is 2.44 ns and is 6.05 ns for the omni/omni case. Therefore, by using a directional antenna at the receiver the minimum RMS delay spread decreased by approximately two and a half times or rather 60% with respect to the value achieved from the omni-directional receiver antenna. When using a directional transmitter and directional receiver antenna the minimum RMS delay spread value decreased by approximately 92% with respect to an omni/omni antenna configuration.

The mean values of σ_τ for the omni/omni, omni/dir, and dir/dir Tx/Rx antenna combinations are 17.34 ns, 11.35 ns, and 7.71 ns, respectively. This corresponds to a 35% decrease and a 55.5% decrease in the mean RMS delay spread with respect to the value obtained from the omni/omni antenna configuration. Overall, the RMS delay spread decreases when directional antennas are introduced into the channel, as expected since the directionality of the beam pattern limits the amount of multipath received by the antenna. Results show that directional antennas used at the receiver or at both transmitter and receiver may help reduce the multipath in the channel as opposed to using omni-directional antennas.

Multipath components were detected with a maximum delay up to 190 ns with respect to the first arrival signal for the omni/omni pair, and 184 ns and 186 ns for the omni/dir and dir/dir antenna combinations, respectively. The average maximum excess delay (i.e., the sample mean value computed over all maximum excess delay values) for the omni/omni, omni/dir, and dir/dir antenna combinations were 143.2 ns, 121.7 ns, and 112.26 ns, respectively. Table 4.3 lists the mean RMS delay spread and mean number of paths N_p for threshold levels of 10 dB, 20 dB, and 30 dB below the maximum component of the PDP and the average percentage of power contained within the PDP for the given threshold levels. From the table it can be concluded that the mean number of paths are considerably reduced for the 20 dB and 30 dB threshold levels as a function of antenna directionality. Even though the number of paths are not as significantly reduced at the 10 dB threshold level for a directional receiver or both Tx/Rx with respect to the omni/omni pair, the mean RMS delay spread is in fact reduced, and at the same time more energy is captured, showing the significance of the directional antennas. In

conclusion, more energy is captured with fewer paths and less dispersion when directional antennas are used at the receiver or both transmitter and receiver as opposed to the omni/omni antenna pair.

Table 4.3. % Power, Mean RMS Delay Spread $\overline{\sigma}_\tau$, and Mean Number of Paths $\overline{N}_p$ for Threshold Levels of 10 dB, 20 dB, and 30 dB Below the Maximum Component

OMNI/OMNI			
Threshold	% Power	$\overline{\sigma}_\tau$ (ns)	$\overline{N}_p$
10 dB	52.50	2.65	4
20 dB	81.80	9.45	31
30 dB	96.30	15.80	86
OMNI/DIR			
Threshold	% Power	$\overline{\sigma}_\tau$ (ns)	$\overline{N}_p$
10 dB	66.80	1.25	2
20 dB	85.90	4.53	13
30 dB	96.25	8.90	48
DIR/DIR			
Threshold	% Power	$\overline{\sigma}_\tau$ (ns)	$\overline{N}_p$
10 dB	81.30	0.36	2
20 dB	91.50	1.11	4
30 dB	96.60	4.75	23

4.2.1 RMS Delay Spread versus Distance

The RMS delay spread of the channel increases as a function of Tx/Rx separation distance as shown in Figure 4.2 on a log-log scale for all three antenna combinations. This has also been observed for indoor and outdoor propagation measurements in [6][12][32]. It has been stated and shown in Chapter 3 that directional antennas highly influence the rate at which path loss increases over distance. As is the case with path loss, the Tx/Rx separation distance has a greater influence on the RMS delay spread when directional antennas are used in the channel as opposed to omni-directional antennas. Therefore, the highest and lowest rates at which path loss and RMS delay spread increase over distance were found to be correlated with one another, where the highest and lowest rates of path loss correspond to the highest and lowest rates of RMS delay spread over distance, respectively. That is, the more directionality introduced into the channel the greater the rate in which path loss and RMS delay spread increase over distance.

Results show that the RMS delay spread for the dir/dir antenna combination increases at the greatest rate over distance followed by the omni/dir pair and lastly the omni/omni pair which increases at the lowest rate with distance. The least squares fit of the RMS delay spread versus distance is shown in Figure 4.2 for each antenna combination, which resulted in the following three distant dependent models: $10 \cdot d^{0.3}$, $4.37 \cdot d^{0.55}$, and $1.32 \cdot d^{1.01}$, for omni/omni, omni/dir, and dir/dir Tx/Rx antenna combinations, respectively, with d in meters. A similar result was obtained for the omni/omni antenna combination in [12], where the RMS delay spread was shown to increase as a function of distance with an exponent of 0.26.

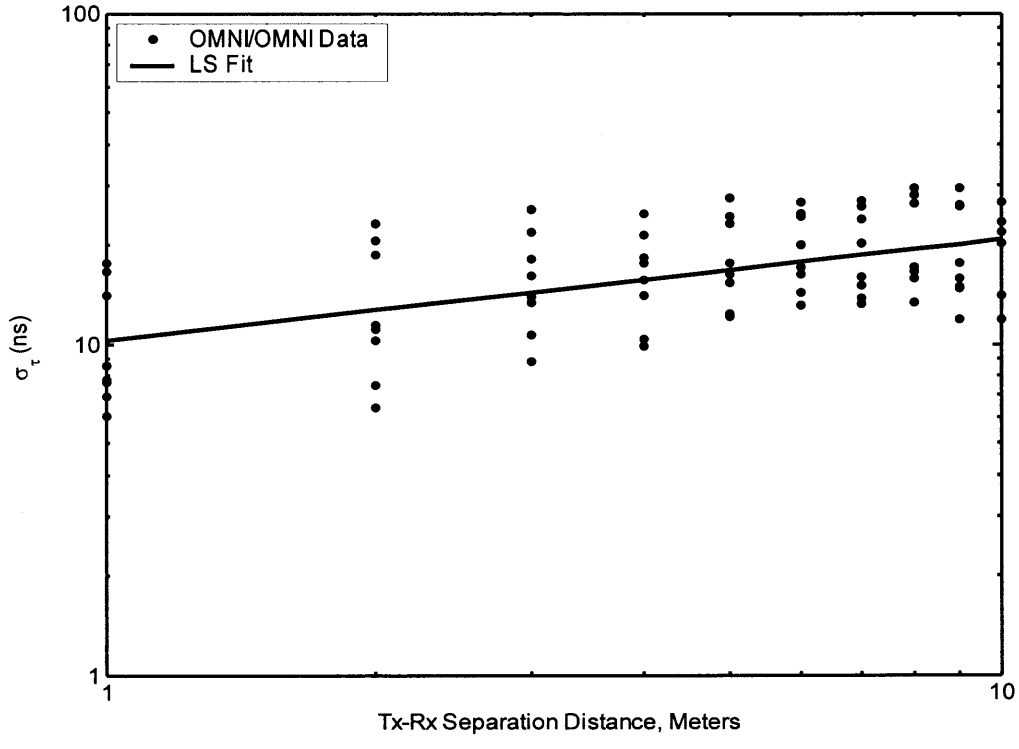

(a)

Figure 4.2. RMS Delay Spread versus Distance. (a) omni-directional/omni-directional. (b) omni-directional/directional. (c) directional/directional.

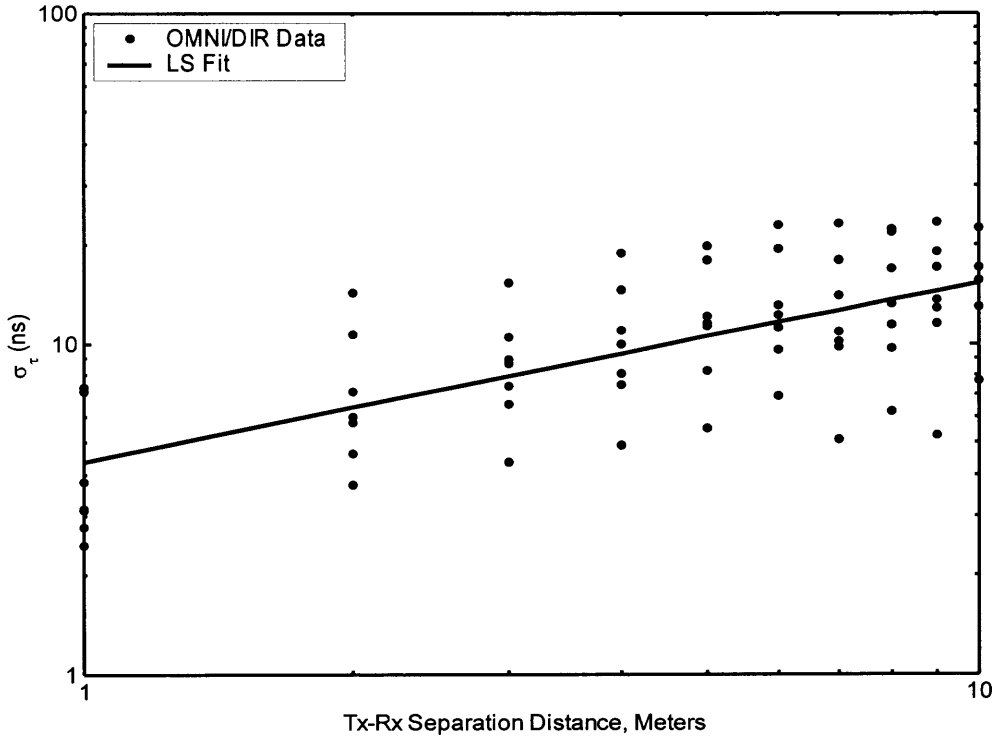

(b)

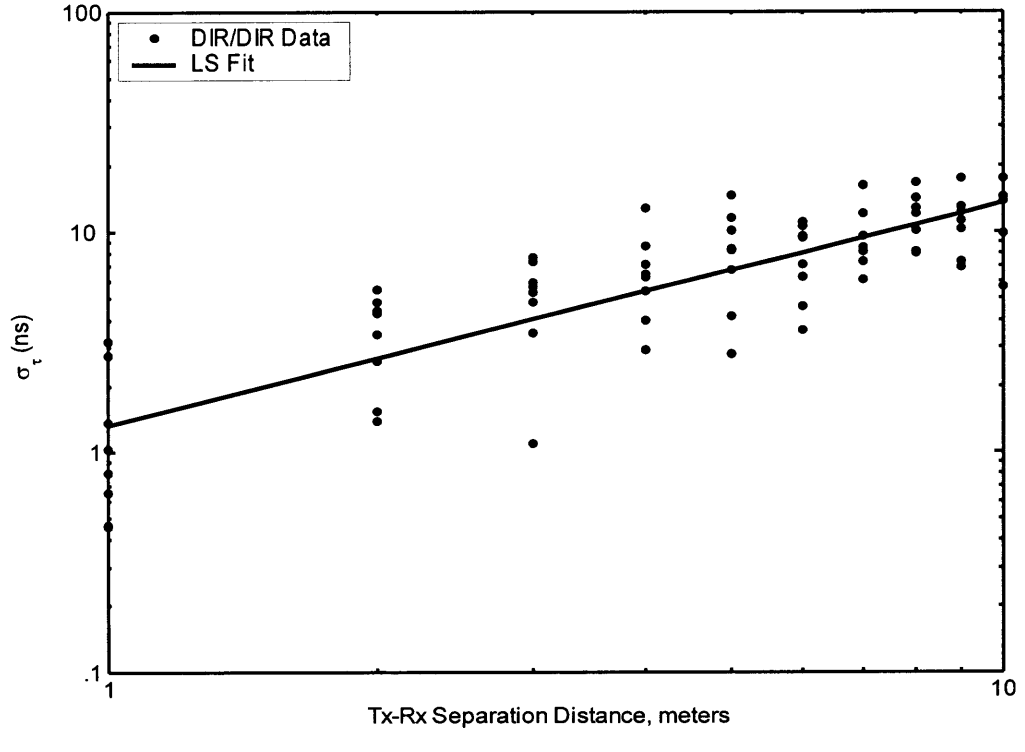

(c)

Figure 4.2. (*Continued*)

4.2.2 Distribution of RMS Delay Spread over Distance

As explicitly stated in Greenstein et al., 1997 [32], the RMS delay spread can be considered to be log-normally distributed at a given distance d. This can be explained starting from the fact that the path loss is log-normally distributed as shown in Figure 3.2, and we can consider the individual power gains of the PDP to be log-normally distributed, which is shown in Chapter 5. Now being that the addition and subtraction of log-normals tend to remain log-normal, and since log-normality is preserved under multiplication, division, powers, and roots it can be concluded that the RMS delay spread is log-normally distributed too [32]. Normal probability plots of the deviation of σ_τ in dB (denoted by s_σ) about the corresponding least squares fit to σ_τ over distance of Figure 4.2 are shown in Figure 4.3. The theoretical normal fit given by the straight line confirms the log-normality of σ_τ over distance. s_σ is a zero-mean normal random variable with a standard deviation denoted by σ_s, with values corresponding to each antenna combination listed in Table 4.4.

As shown in Table 4.4, σ_s becomes greater with antenna directivity. Therefore, larger deviations of RMS delay spread can be expected with respect to the mean at a given distance d for directional antennas as opposed to omni-directional antennas. This implies that directional antennas are more sensitive to multipath dispersion than omni-directional antennas at different locations with the same Tx/Rx separation distance. This is a valid result and can be explained from a physical point of view. It is known that multipath components are significantly reduced in the channel when directional antennas are used. Not only are signals rejected when arriving within the null point of the

radiation pattern, but are also attenuated greatly by the antenna side lobes. On the other hand, omni-directional antennas are unable to reject multipath

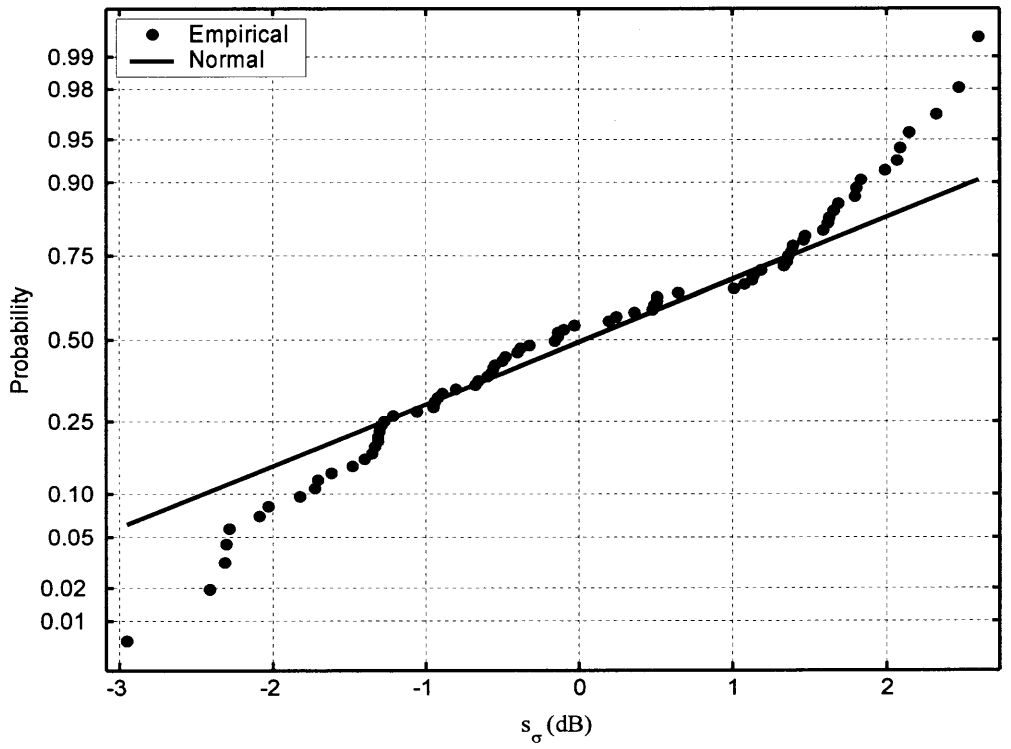

(a)

Figure 4.3. Deviation of σ_τ over distance about the least squares fit. (a) omni-directional/omni-directional. (b) omni-directional/directional. (c) directional/directional.

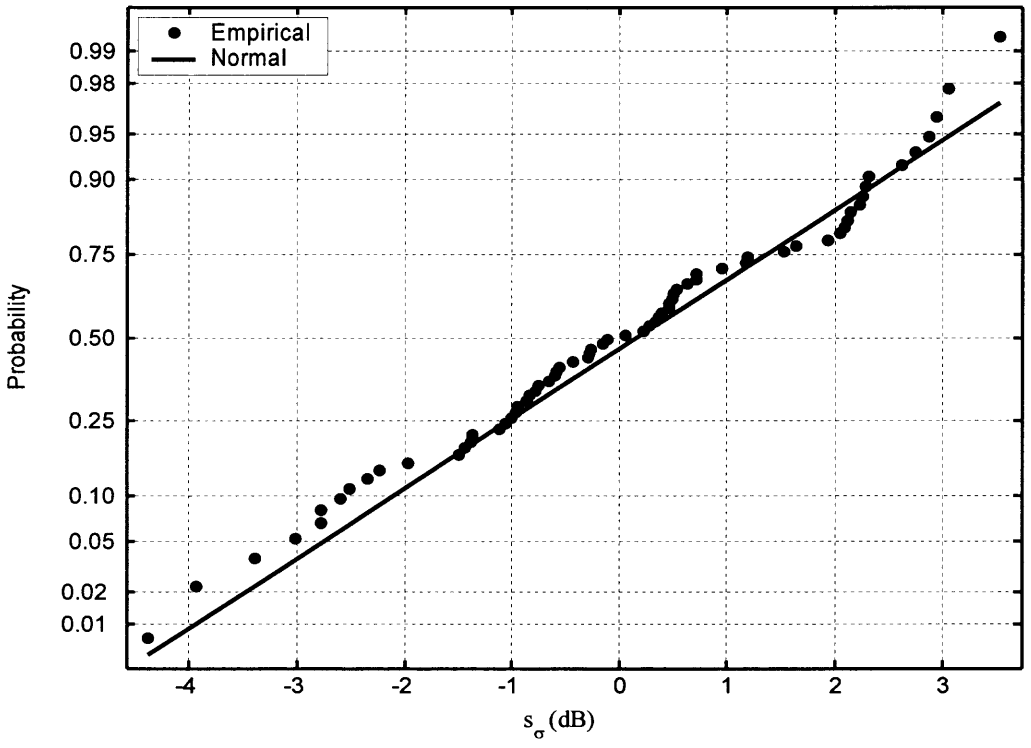

(b)

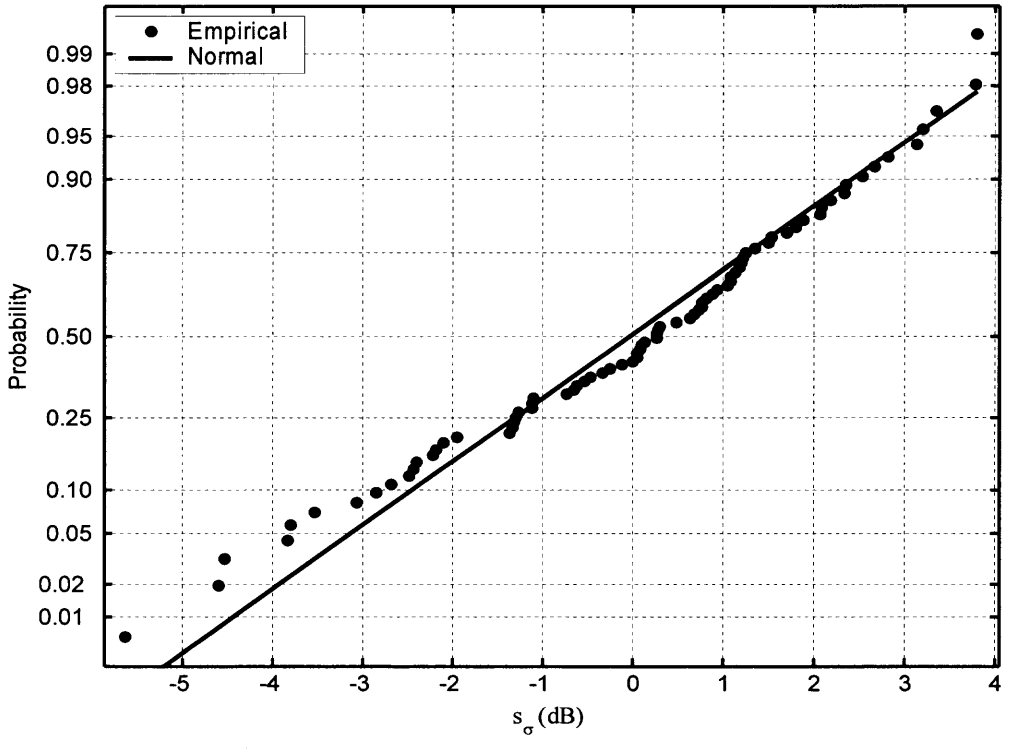

(c)

Figure 4.3. (*Continued*)

Table 4.4. Standard Deviation of s_σ For Each Antenna Combination

Antenna Combination	σ_s (dB)
OMNI/OMNI	1.43
OMNI/DIR	1.82
DIR/DIR	2.06

components and thus all multipath arriving within a 360° radius of the antenna are accepted. Let us define an outlier as a multipath component that is either highly attenuated or highly accentuated with respect to the norm, which results in a large deviation about the mean RMS delay spread at a given distance. The chances of a directional antenna receiving an outlier are much more probable then omni-directional antennas since multipath components arriving at different angles are subject to different gain levels of the radiation pattern. The omni-directional antenna exhibits a constant gain beam pattern and all multipath signals are ideally attenuated equally when arriving at different angles. Therefore, the RMS delay spread is more likely to deviate about the mean when directional antennas are used in the channel as opposed to omni-directional antennas.

4.2.3 Correlation Between Shadow Fading and RMS Delay Spread

The path loss and RMS delay spread are both inherently dependent on the received multipath in the channel. Therefore, it can be inferred that a change in the path loss corresponds to some change in the RMS delay spread. It was postulated and shown in [32] that when a deep shadow fade occurs the RMS delay spread tends to increase for

digital cellular environments. That is, deep shadow fades are more likely to be correlated with larger RMS delay spread values.

When considering different channels, one may expect a channel corresponding to the greatest shadow fading variance (deviation in path loss) to correspond to the greatest deviation of σ_τ, which is not true when considering different antenna combinations. This was shown in the previous section, where the dir/dir antenna combination resulted in the smallest shadow fading variance and the largest variance in RMS delay spread and vice versa for the omni/omni antenna pair. Therefore, the largest standard deviation of the shadow fading random variable does not necessarily correspond to the largest standard deviation of the RMS delay spread over distance when comparing different channels, but rather the largest shadow fading deviation for a given channel (i.e., greatest path loss) at a given distance d should correspond to the largest RMS delay spread deviation at that distance d.

Therefore, analysis is carried out on the correlation between shadow fading and RMS delay spread for each antenna combination to assess the interdependency between the two variables. This is done by analyzing the influence shadow fading has on the RMS delay spread values. A quantitative measure of the correlation between two variables and the influence they have on one another is given by the correlation coefficient denoted by ρ. When a deep shadow fade occurs the path loss increases and from the previously stated conjecture we can expect an increase in RMS delay spread, which results in a positive value for ρ. The correlation coefficient is given by,

$$\rho = \frac{\overline{XY}}{\hat{\sigma}_X \hat{\sigma}_Y} \tag{4.7}$$

where X and Y correspond to the shadow fading random variable X and RMS delay spread σ_τ, respectively. $\hat{\sigma}_X$ and $\hat{\sigma}_Y$ are standard deviations estimated from the data. Figure 4.4 shows the RMS delay spread versus shadow fading for each antenna combination. Note that positive shadow fading values in Figure 4.4 correspond to an increase in path loss with respect to the MMSE fitted response of Figure 3.1. The values of ρ for each antenna combination are listed in Table 4.5.

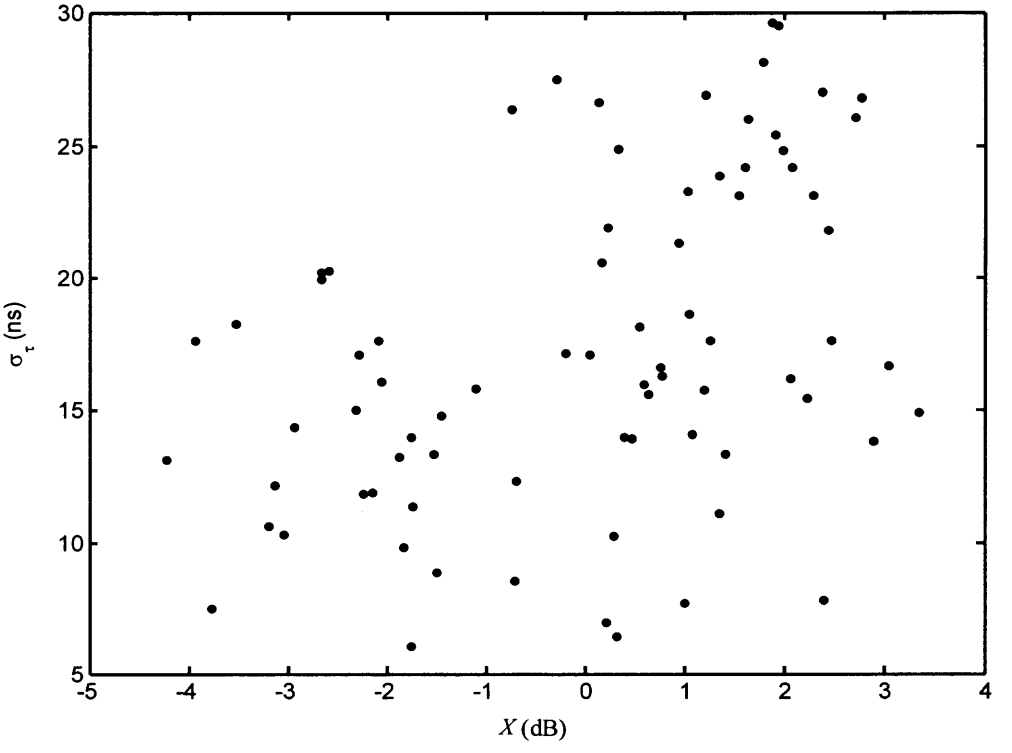

(a)

Figure 4.4. Shadow fading versus RMS delay spread. (a) omni-directional/omni-directional. (b) omni-directional/directional. (c) directional/directional.

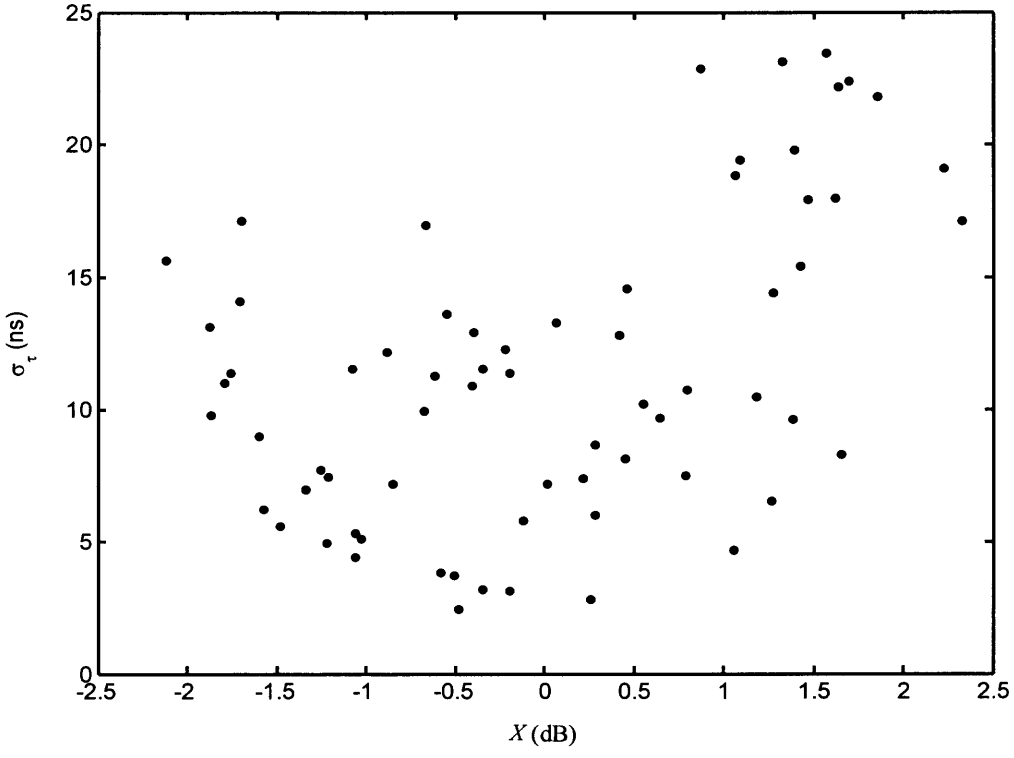

(b)

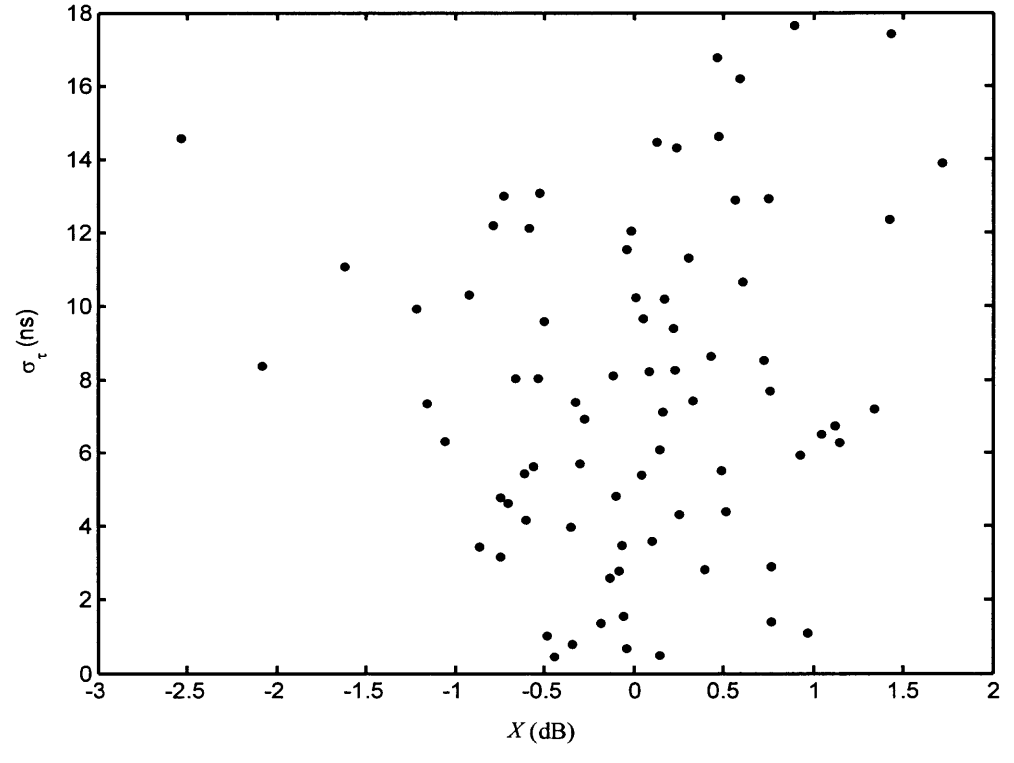

(c)

Figure 4.4. (*Continued*)

Table 4.5. Correlation Coefficient Between Shadow Fading and RMS Delay Spread

Antenna Combination	ρ
OMNI/OMNI	.42
OMNI/DIR	.47
DIR/DIR	.10

Results show that deep shadow fades (e.g., a drop in total power about the mean) tend to be correlated with larger RMS delay spread values for the omni/omni and omni/dir antenna combinations. On the other hand, there is a small correlation between deep shadow fading and larger RMS delay spread values for the dir/dir antenna combination. Overall results show positive correlation for all three cases, which indicates that the channel is more likely to suffer a fading loss and an increase in RMS delay spread about the mean simultaneously.

The dir/dir antenna combination does not show much correlation, which can be explained by the fact that multipath arrivals are sparsely distributed over delay and the power gain of each arrival is highly dependent on the angle of arrival with respect to the maximum gain region of the antenna. The multipath in the channel appears to arrive in clusters, which is explained in Chapter 5, and this being the case has a double effect on the RMS delay spread when power levels are above and below the mean value. Therefore, if multipath arrivals are more attenuated at lower delays the later arrival components will increase the RMS delay spread value. That is, a loss in total power results in a larger RMS delay spread value. On the other hand, if a later arrival

component arrives within the main beam of the antenna the total power will increase and the RMS delay spread will increase. If a late arriving component does not exist then the total power will drop below the mean value and the RMS delay spread will decrease. Lastly, if more power exists for early arrivals then a late arriving component will not have a great effect on the RMS delay spread and thus the RMS delay spread can be expected to decrease. All cases are plausible given the limited amount of multipath and the dependency the arrival angles have on the power gains due to the non-uniform antenna gain of the radiation pattern.

An omni-directional antenna creates more multipath in the environment and therefore when a change occurs in the total received power it is most likely a result of a change in the power gain of the lower delayed multipath components as opposed to longer delayed multipath components. This is possible since longer delayed pulses do not carry significant power compared to the power contained in the LOS and lower delayed multipath component arrivals. Therefore, when lower delayed multipath components become attenuated the later arrivals will cause the RMS delay spread to increase and vice versa [32]. This explains why a loss in power can be correlated with a larger RMS delay spread value and a gain in power can be correlated with lower RMS delay spread values.

The omni/dir antenna combination exhibits the highest correlation with the omni/omni antenna combination corresponding to a slightly lower value. A possible explanation for this is that when lower delayed arrivals are attenuated as seen from the omni-directional antenna, the directional antenna causes further attenuation due to the side lobes as explained previously. Thus, the RMS delay spread can be expected to be

more sensitive to this, since less multipath is captured from the directional antenna as compared to the omni-directional antenna.

4.3 Summary

In this chapter, the time domain statistics of the channel were thoroughly analyzed for each antenna combination. Results show that the mean, minimum, median, and maximum RMS delay spread values have all decreased as a function of antenna directivity in the channel. Therefore, the lowest values were obtained for the dir/dir antenna combination and the highest values were obtained for the omni/omni antenna combination. All antenna combinations show a power law relationship between RMS delay spread and distance, with results for the dir/dir antenna pair increasing at the greatest rate followed by those for the omni/dir antenna pair and finally those for the omni/omni antenna pair. The RMS delay spread deviation over distance was shown to be greatest for the dir/dir antenna pair followed by the omni/dir antenna pair, with the smallest deviation being for the omni/omni antenna pair. This proves that directional antennas are more affected by changes in multipath propagation at different locations for a given distance d. That is more variation in the RMS delay spread can be expected when directional antennas are used as opposed to omni-directional antennas.

Results show that shadow fading tends to be correlated with RMS delay spread values for omni/omni and omni/dir antenna combinations. That is, when a deep shadow fade occurs, the RMS delay spread can be expected to increase. On the other hand, the dir/dir antenna combination did not show a significant amount of correlation between shadow fading and RMS delay spread. Therefore, deep fades are not necessarily

associated with larger RMS delay spread values when a directional transmitter and directional receiver are used in the channel. The highest correlation was achieved for the omni/dir antenna combination.

CHAPTER 5

CHANNEL IMPULSE RESPONSE MODEL

The received signal in the measured environment consists of many multipath signals arriving at the receiver antenna. This is caused from the transmitted signal taking on multiple paths from the ground, walls, ceiling, doors, and clutter in the environment. Multipath signals can be represented as dirac delta functions weighted by the associated path gain, resulting in a discrete impulse response representation of the channel. In this chapter, a distance-dependent discrete impulse response model of the channel is presented.

5.1 General Impulse Response Model Representation

As mentioned previously, when a signal is transmitted into the wireless medium, multiple radiowaves are received from multiple propagation paths. This phenomenon is most commonly referred to as multipath propagation. Multipath signals in the propagation channel can be represented as Dirac delta functions weighted by the power in each multipath component, resulting in a discrete impulse response of the channel $h(\tau;d)$ as mentioned in Chapter 4, which is shown below for convenience.

$$h(\tau;d)=\sum_{i=0}^{N-1} a_i(\tau;d)e^{j\theta_i(\tau;d)}\delta(\tau-\tau_i). \tag{5.1}$$

The PDP of the channel can be represented as,

$$P(\tau;d)=\sum_{i=0}^{N-1}\left|a_i(\tau;d)\right|^2\delta(\tau-\tau_i). \tag{5.2}$$

which was also explained in Chapter 4. The normalized PDP is denoted as P_{norm} and is given by,

$$P_{norm}(\tau;d) = \frac{P(\tau;d)}{\sum_{i=0}^{N-1} P(\tau_i;d)}, \tag{5.3}$$

where,

$$\sum_{i=0}^{N-1} P(\tau_i;d) = PL(d). \tag{5.4}$$

Therefore, the channel power at a distance d computed using Equation (5.4) is equivalent to Equation (3.1) where the channel power is computed in the frequency domain. This mathematical relationship is known as *Parseval's theorem* [30].

P_{norm} can be represented as,

$$P_{norm}(\tau;d) = \frac{P(\tau;d)}{PL(d)}. \tag{5.5}$$

Therefore, the PDP of the channel can be written as,

$$P(\tau;d) = PL(d) \cdot P_{norm}(\tau;d) = PL(d) \sum_{i=0}^{N-1} P_{norm}(\tau_i;d)\delta(\tau - \tau_i). \tag{5.6}$$

By taking the square root of Equation (5.6) and including the associated phase information corresponding to each ith multipath component, the impulse response of the channel given by Equation (5.1) can we written as [13],

$$h(\tau;d) = \sqrt{PL(d)} \sum_{i=0}^{N-1} \sqrt{P_{norm}(\tau_i;d)} e^{j\theta_i(\tau;d)} \delta(\tau - \tau_i). \tag{5.7}$$

As shown in Equation (5.7) the discrete channel impulse response can be represented using a model for the path loss and a model for the normalized PDP. Equation (5.7) is the basis of the statistical channel impulse response model or rather is shown in general

form with no specific channel characteristics explaining the behavior of the channel. To statistically generate impulse responses of the channel, the path loss over distance and a model of the normalized PDP must be characterized and integrated into Equation (5.7). A statistical path loss model for $PL(d)$ has been described in Chapter 3, and a statistical model of P_{norm} is described in section 5.3, which completes all model information needed to statistically characterize the channel impulse response of Equation (5.7).

5.2 Channel Impulse Response Measurements

5.2.1 Conjectures of Impulse Response Measurements

Figure 5.1a is a typical normalized channel impulse response (CIR) measured at 6 m in the EE laboratory using an omni-directional/omni-directional antenna combination. Figures 5.1b and 5.1c represent the normalized channel impulse response at the same location as the CIR of Figure 5.1a using omni-directional/directional and directional/directional antenna combination pairs, respectively. Figure 5.2 represents channel impulse response measurements taken at 4 m in the classroom for each antenna combination. The CIR measurements shown in Figures 5.1 and 5.2 both exemplify a similar channel behavior in which the multipath in the channel appears to arrive in clusters. The impulse response measurements shown in these figures were measured in different rooms, suggesting that the channel reacts in a similar manner amongst different rooms. This similar channel behavior can be deduced from the fact that the measured rooms consist of homogeneous environmental characteristics and thus should result in similar impulse response measurements.

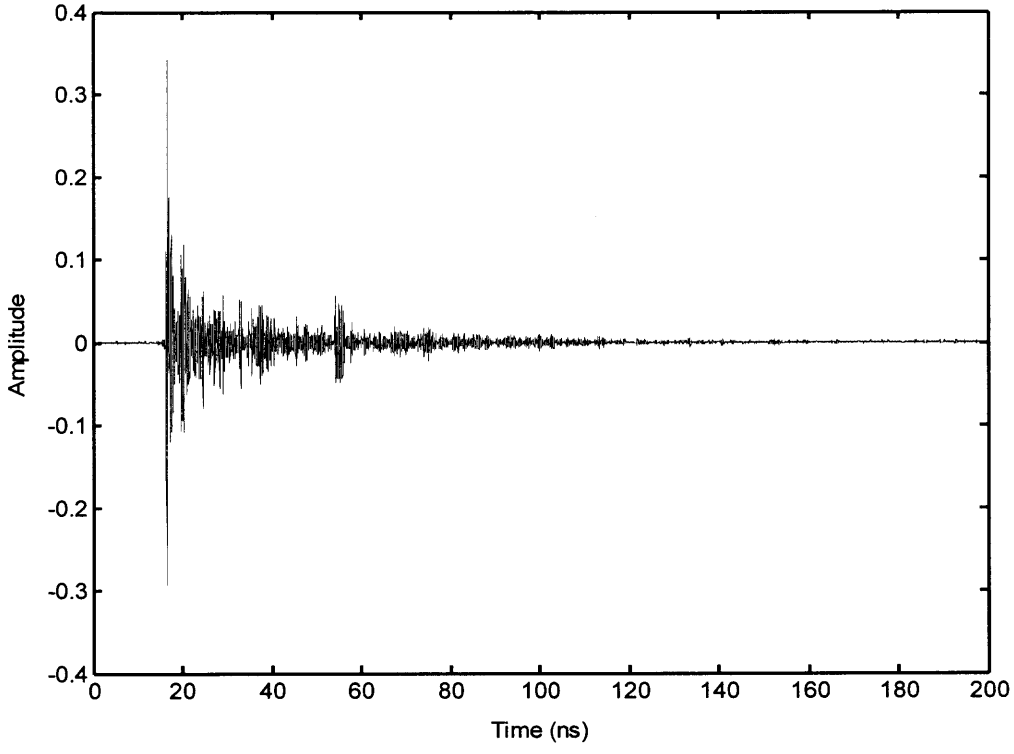

(a) omni-directional/omni-directional

Figure 5.1. Normalized channel impulse response measurements at 6 m in the EE laboratory. (a) omni-directional/omni-directional. (b) omni-directional/directional. (c) directional/directional.

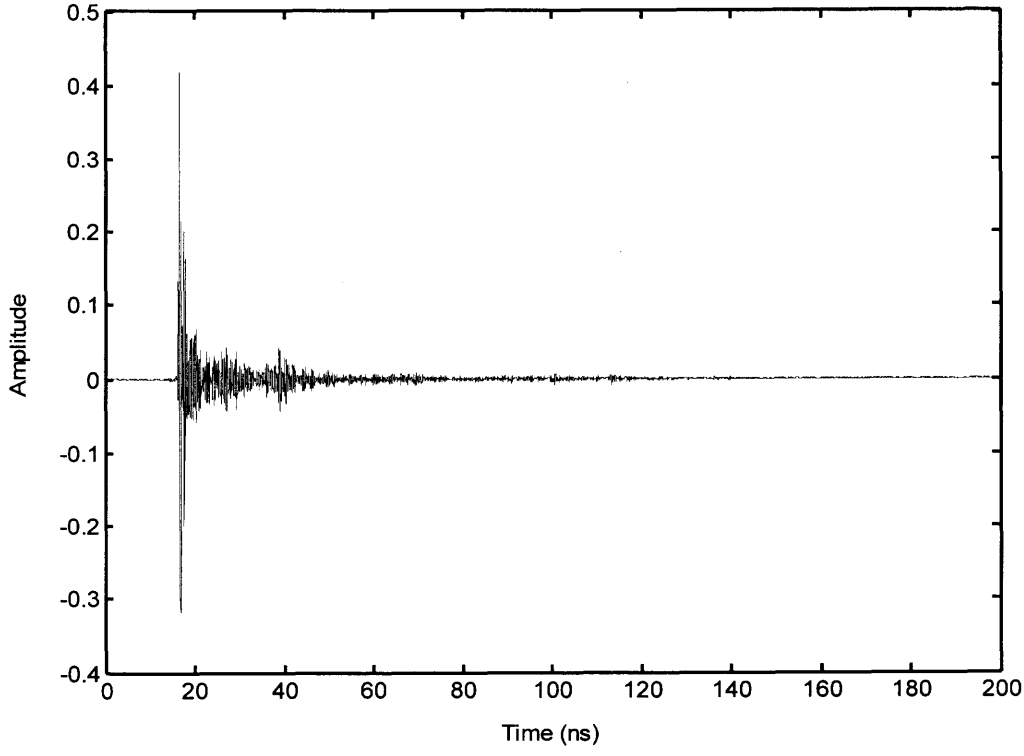

(b) omni-directional/directional

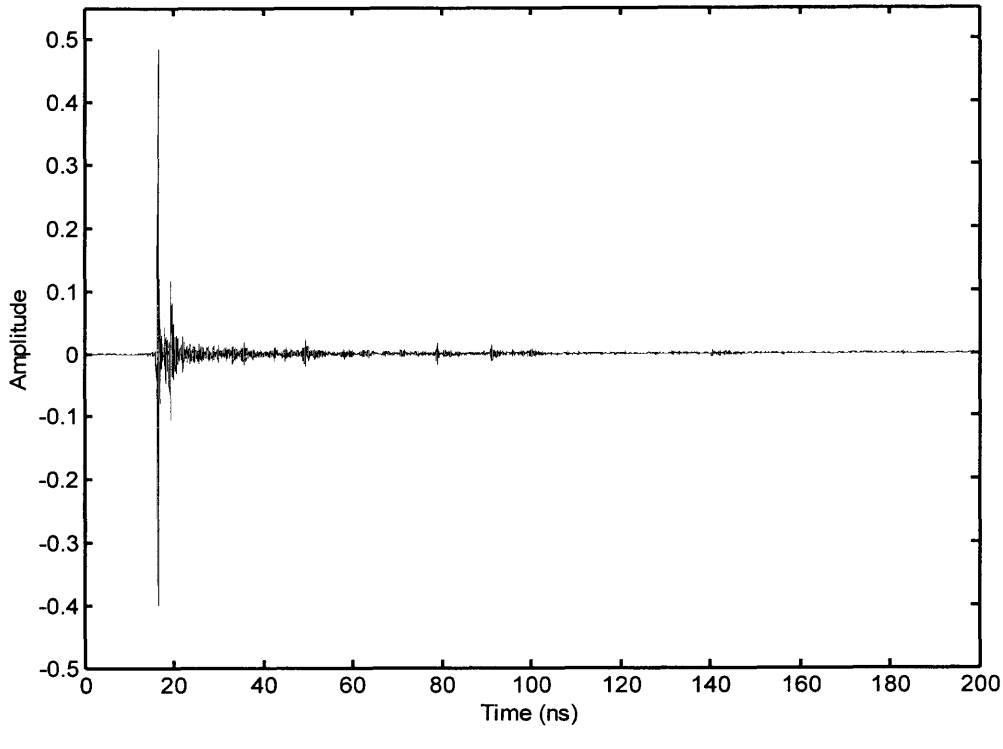

(c) directional/directional

Figure 5.1. (*Continued*)

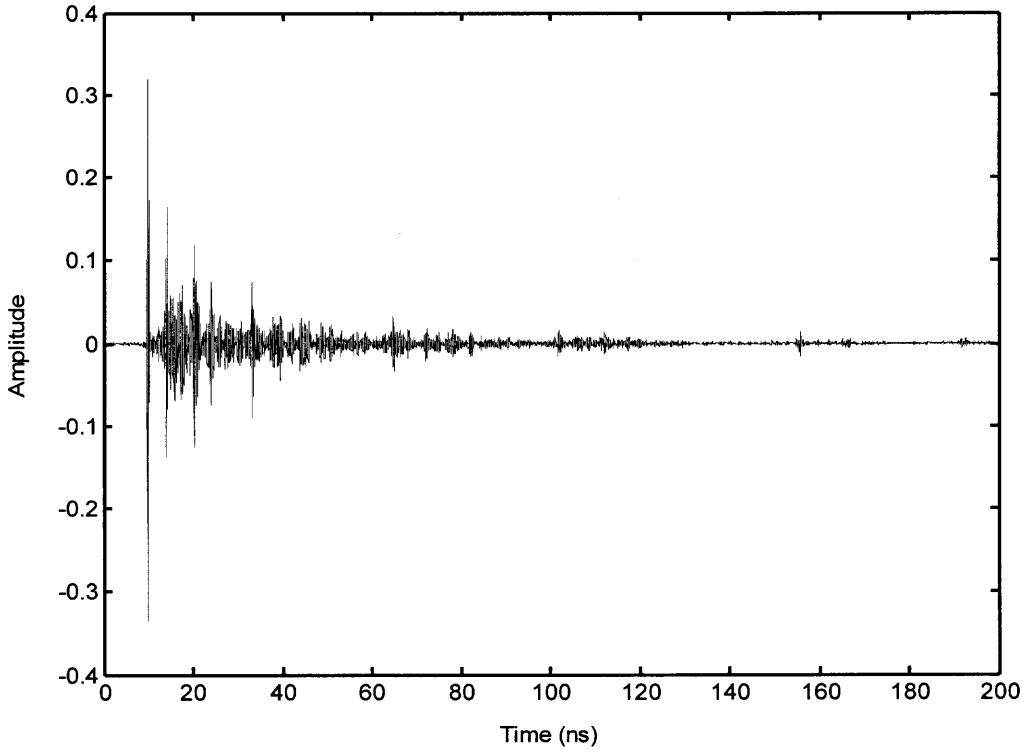

(a) omni-directional/omni-directional

Figure 5.2. Normalized impulse response measurements at 4 m in the classroom. (a) omni-directional/omni-directional. (b) omni-directional/directional. (c) directional/directional.

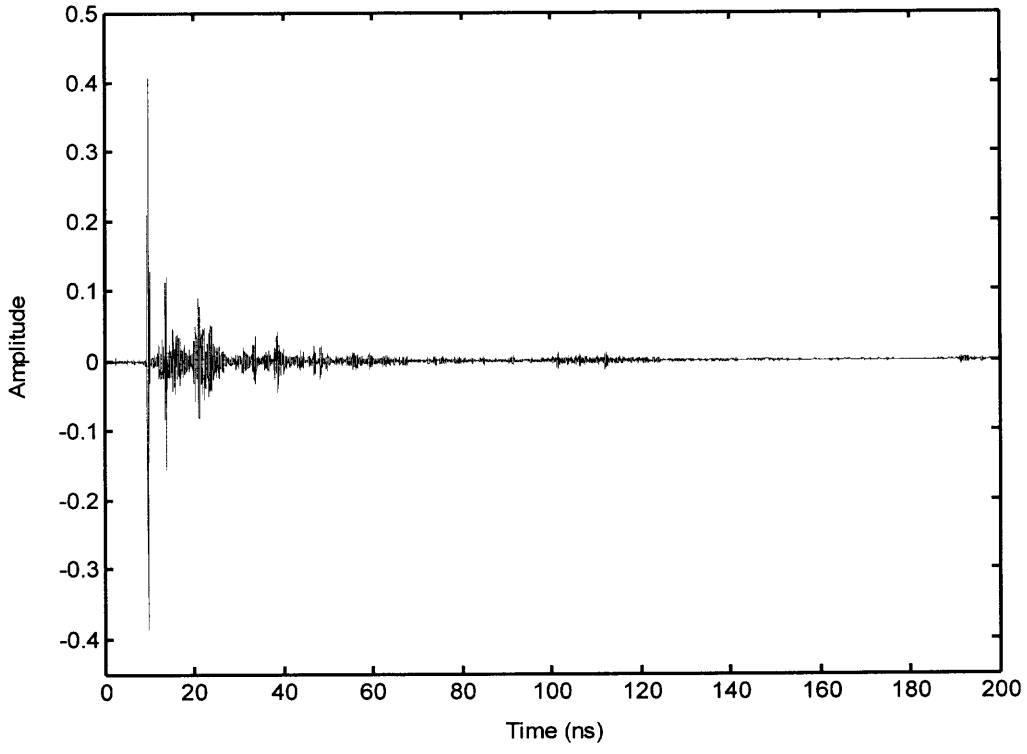

(b) omni-directional/directional

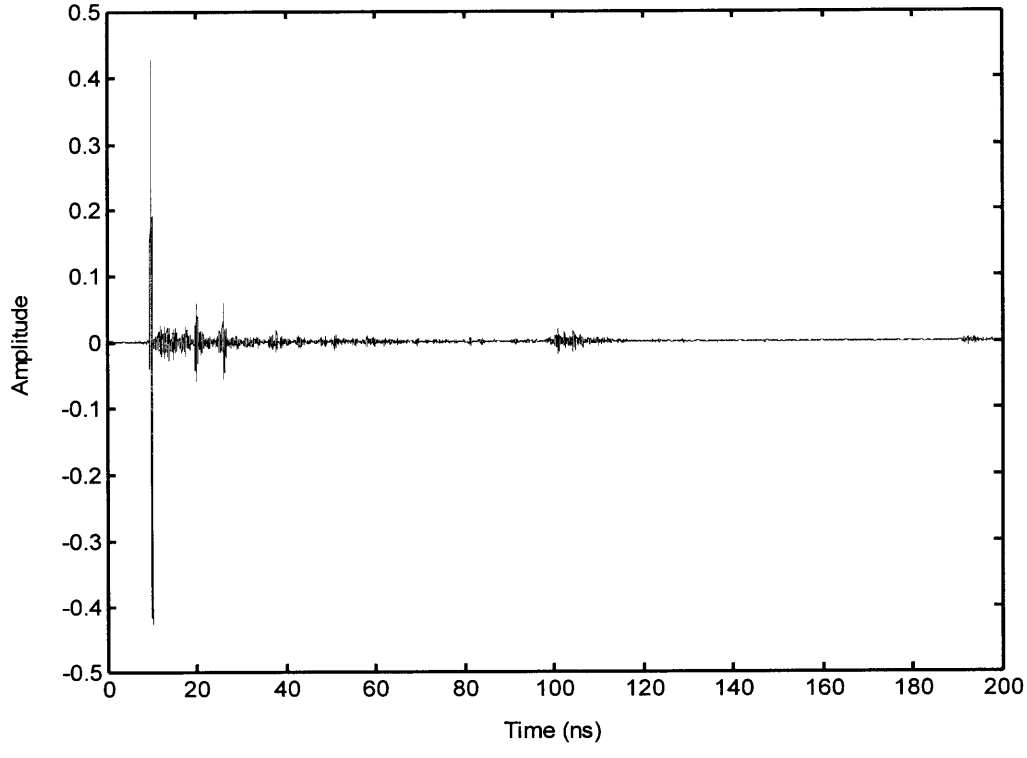

(c) directional/directional

Figure 5.2. (*Continued*)

The normalized CIR is given by,

$$h_{norm}^{(k)}(t;d) = \left(\sqrt{\sum_{i=0}^{P-1} |h_k(t_i;d)|^2} \right)^{-1} \cdot h_k(t;d), \tag{5.8}$$

where P represents the total number of samples of $h_k(t;d)$, t_i is the time delay of the i^{th} sample, k denotes the k^{th} snapshot, and d is the aforementioned Tx/Rx separation distance in meters. Note that the impulse response is a function of t in this case and not τ, which is associated with the binned data. Therefore, $h_k(t;d)$ is a direct result of the IFFT of the frequency response of the channel $H_k(f;d)$.

As mentioned in Chapter 3, the frequency response was measured with respect to a distance of 1 m inside an anechoic chamber. Therefore, the effects of the measurement system apparatus are cancelled out, resulting in a time domain response solely dependent on the effects of the channel. With this in mind, note that the time domain response of Figures (5.1a)-(5.1c) each begin with a time delay of approximately 16.5 ns. This time delay is governed by the fact that the LOS signal traveled a distance of 6 m and was then time shifted back with respect to the calibration distance of 1 m. Therefore, this time delay is given by the signal traveling at the speed of light (i.e., $3\times10^8 \text{m/s}$) over a relative distance of 5 m resulting in approximately 16.67 ns.

The channel impulse response measurements illustrated in Figures 5.1 and 5.2, each consist of a large first arrival signal (e.g., LOS signal) with respect to subsequent multipath arrivals. After the first arrival signal, multipath components appear to arrive in clusters. Similar channel characteristics have been observed in previous wireless channel propagation studies. For example, the clustering phenomenon of multipath arrivals has been observed for wideband indoor measurements taken inside a medium size office

building [11]. However, the statistical channel model in [11] is representative of a non-LOS channel and thus does not include the existence of a relatively large LOS path. In other case studies, for indoor and outdoor measurements, a large first arrival signal has been shown to exist in the channel [13][17][31], but without the effect of multipath signals arriving in clusters and rather having a single cluster arrival immediately following the first arrival. Although there are differences, a similarity amongst all four cases mentioned is that the rays of the clusters all experience an exponential decay over time. In this thesis the PDP of the channel is a function of a large LOS component plus multipath clusters which decay exponentially and contain rays which decay exponentially within the clusters. This appears to be similar to the channel characteristics of Saleh-Valenzuelza [11] and Ghassemzadeh [13], or rather a combination of the two. Although similarities do exist, these two models are not entirely explicative of the measured data in this thesis. Therefore, if used separately, the models will not capture the effect of the channel impulse response presented here and thus modifications are needed.

5.2.2 Effects of Antenna Directionality on Power Delay Profiles

Ten normalized power delay profiles corresponding to the impulse response measurements of Figure 5.2 are shown on a dB scale in two 3-dimensional views in Figure 5.3. In other words, ten PDP measurements (or snapshots) taken at a single location at 4 m in the classroom are shown in two plots for each antenna combination. Two plots of the data are shown for each antenna combination to view the PDP measurements at different angles. It is evident from Figure 5.3, that the multipath in the channel has decreased as a result of antenna directionality.

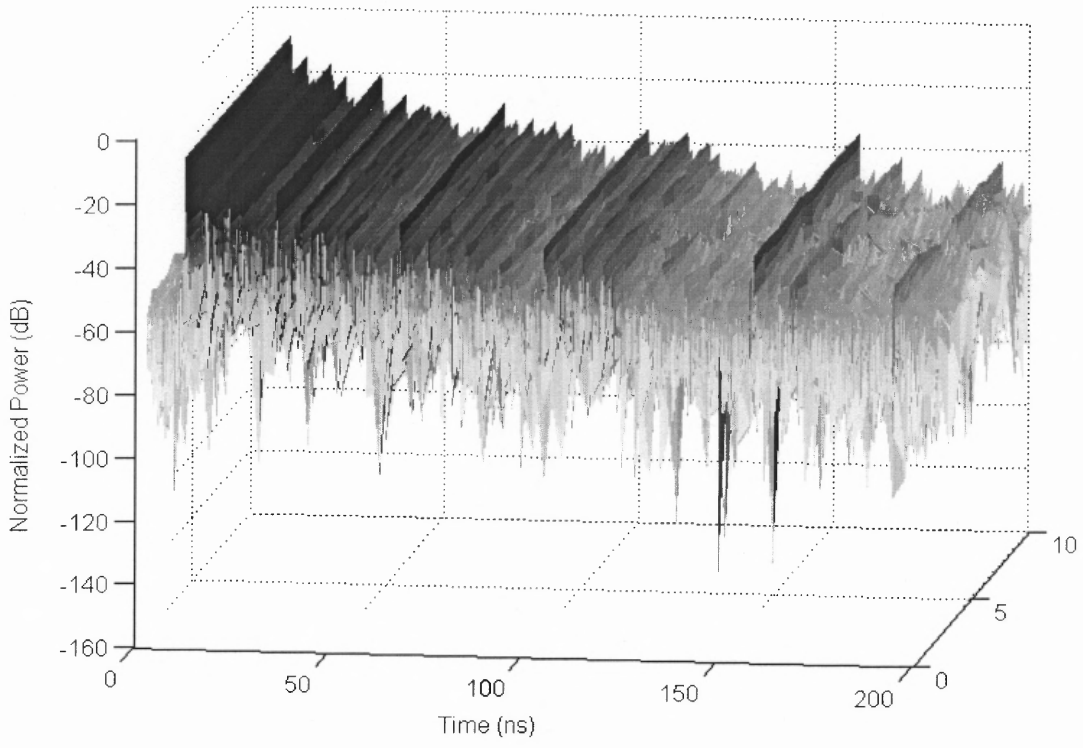

(a.1) omni-directional/omni-directional

Figure 5.3. Ten normalized PDP measurements at a 4 m location in the classroom shown in two 3-dimensional views. (a.1 & a.2) omni-directional/omni-directional. (b.1 & b.2) omni-directional/directional. (c.1 & c.2) directional/directional.

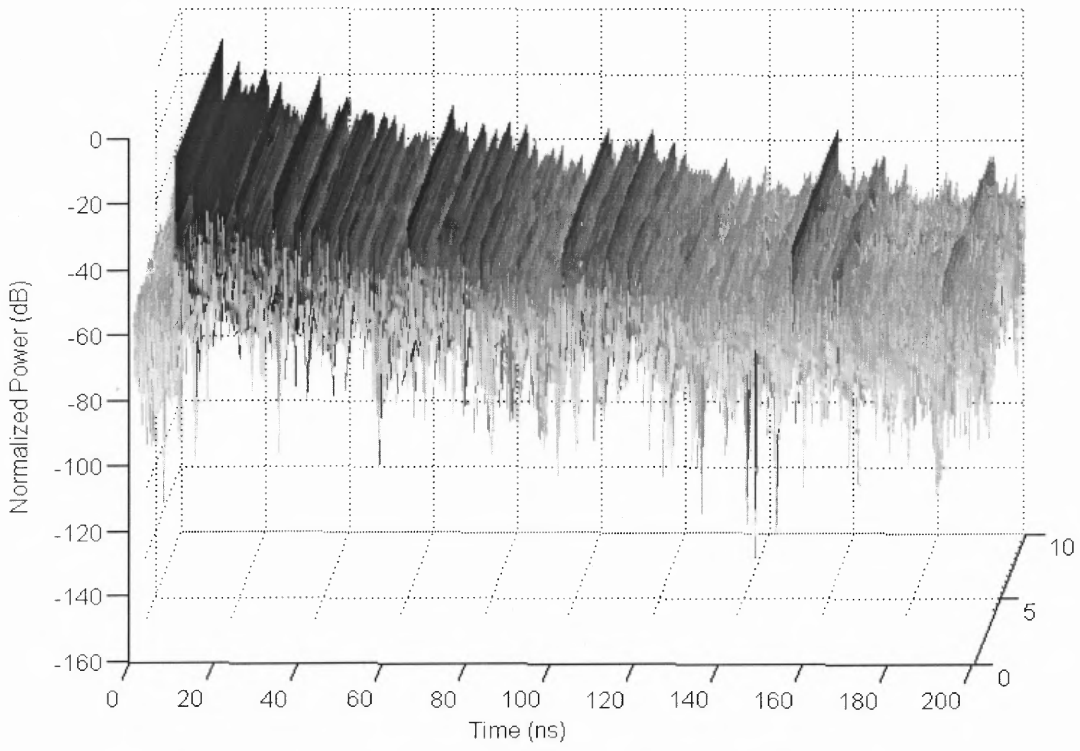

(a.2) omni-directional/omni-directional

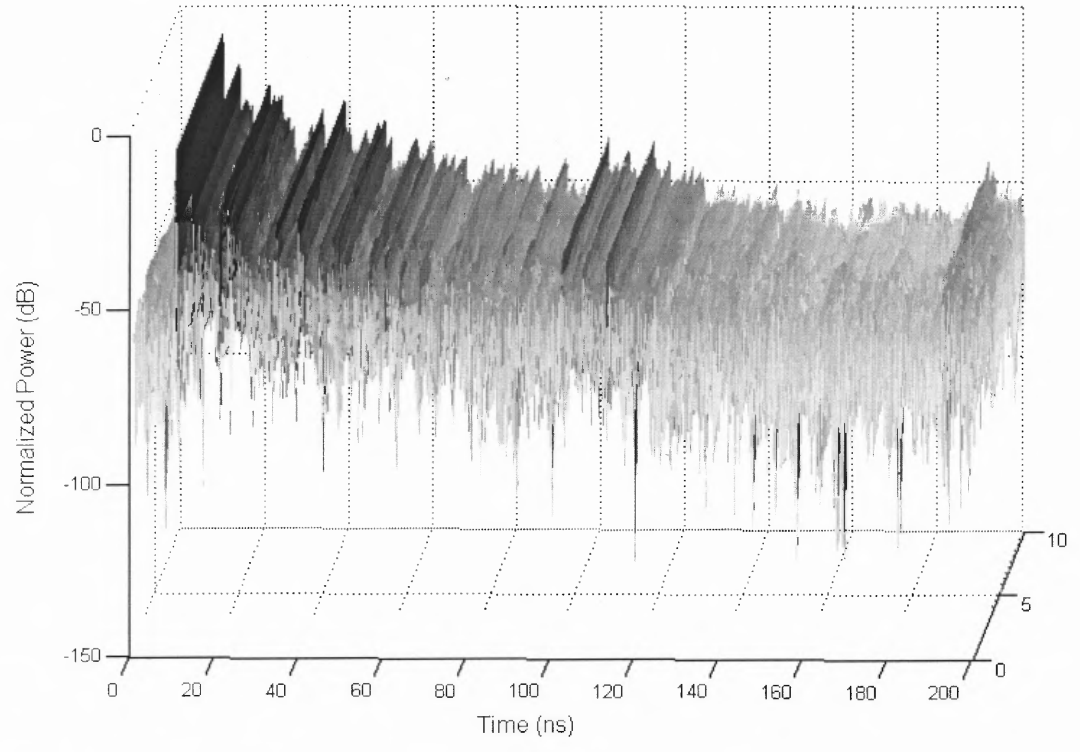

Figure 5.3. (*Continued*). (b.1) omni-directional/directional

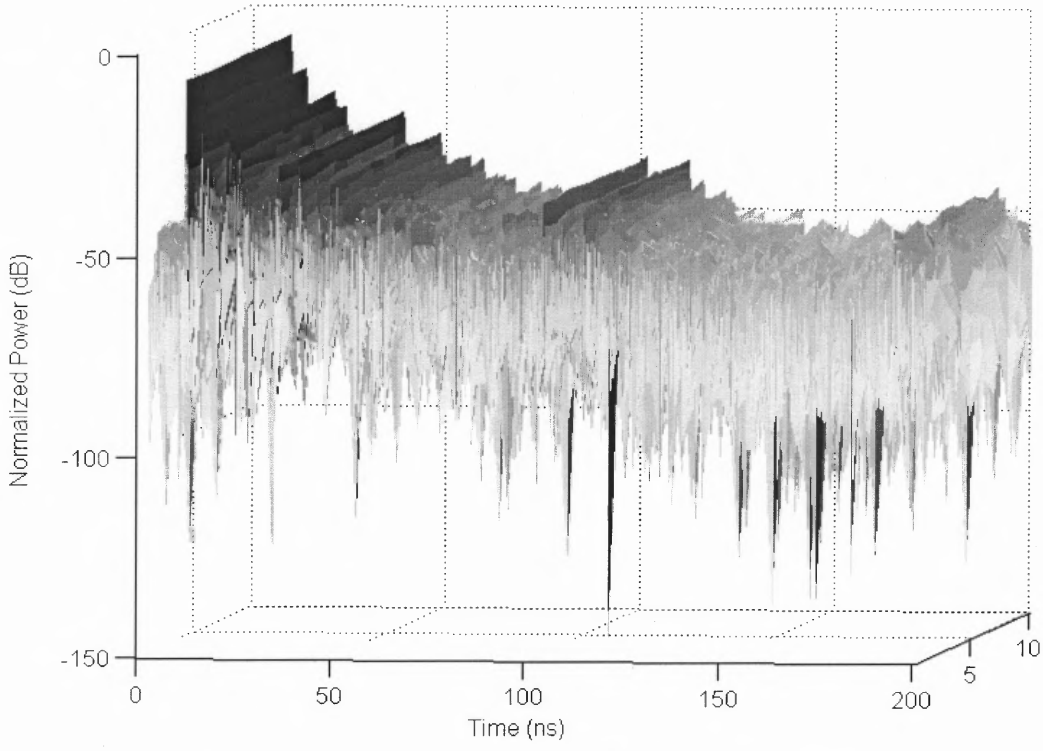

(b.2) omni-directional/directional

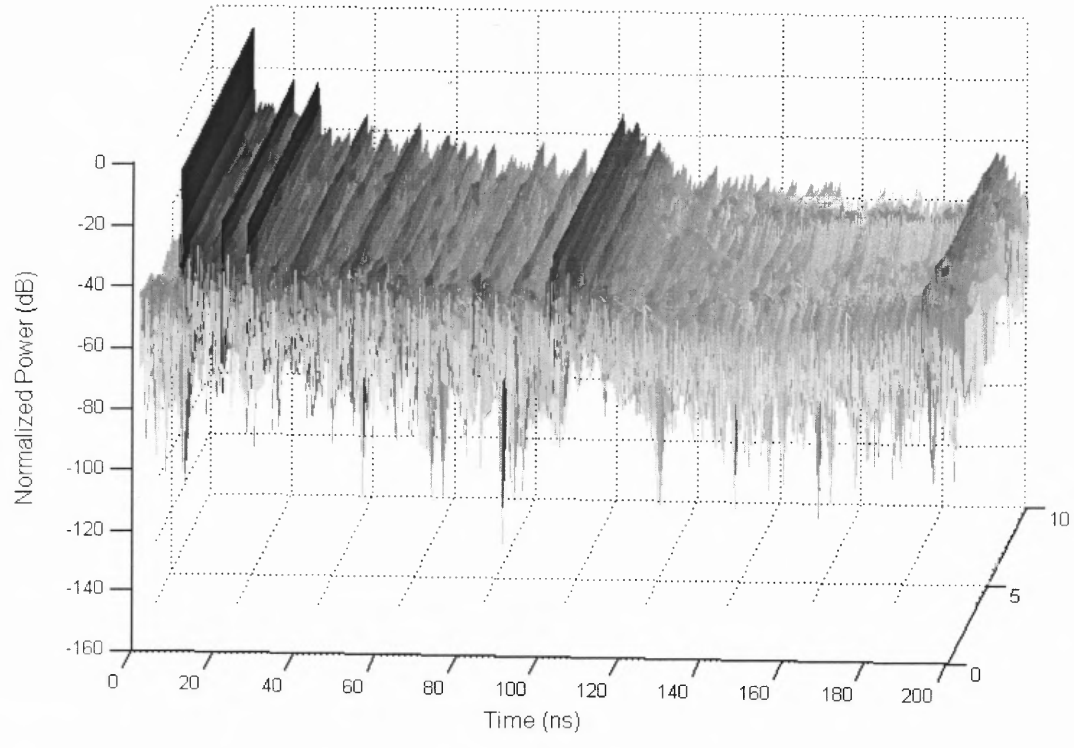

Figure 5.3. (*Continued*). (c.1) directional/directional

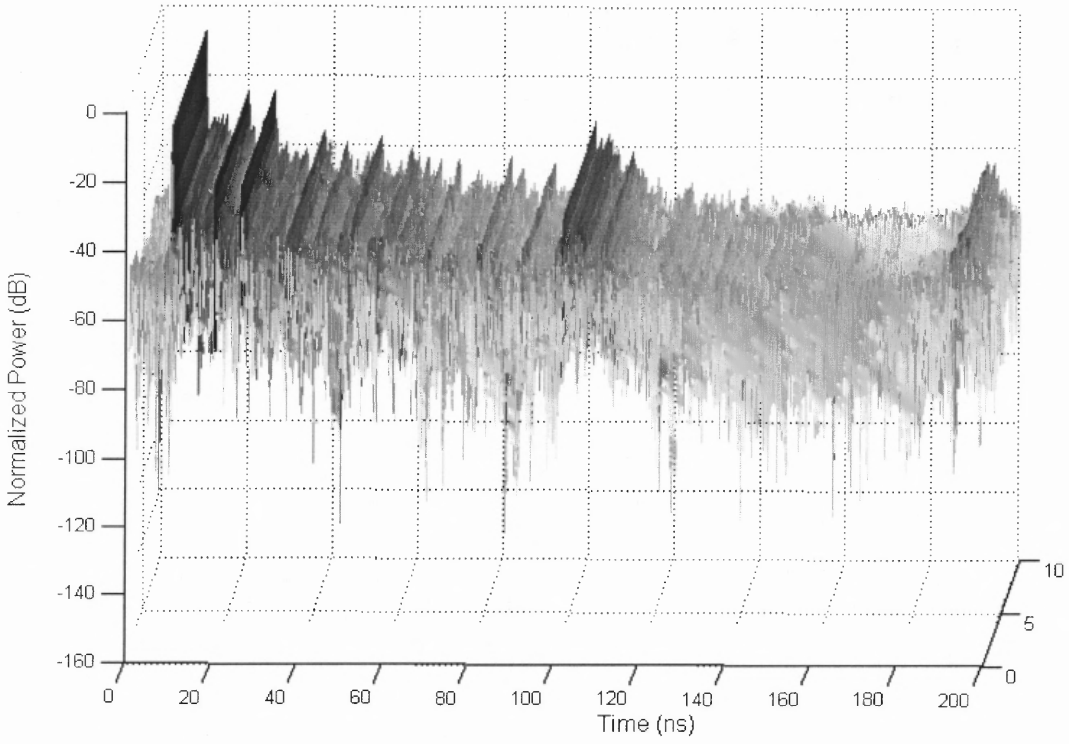

(c.2) directional/directional

Figure 5.3. (*Continued*)

The directional antennas produce a spatial filtering effect, in which signals are only received or transmitted within a specific region of space, dependent on the antenna radiation pattern. Therefore, when using a directional antenna at the receiver instead of an omni-directional antenna, the amount of multipath received in the channel decreases as a result of the sectorization of the radiation pattern of the antenna. This is shown in Figure 5.3, where plots a.1 and a.2 correspond to an omni/omni antenna combination and plots b.1 and b.2 correspond to an omni/dir antenna combination. For example, the multipath present at approximately 150 ns in Figure 5.3 (a.1 and a.2), has been completely rejected by the directional receiver antenna giving a clear visualization of the spatial filtering effect of directional antennas.

Although, the channel is dissimilar at some time instances due to different antenna combinations, there is a multipath arrival time correlation amongst all plots of Figure 5.3. This is expected since the surrounding environment has not changed and multipath components arriving in the antenna beam of an omni-directional antenna will partially be detected by a directional antenna, resulting in correlated multipath arrivals. From a receiver point of view the omni-directional antenna collects multipath signals arriving within a 360° radius of the antenna and thus cannot eliminate multipath arrivals from any direction. The radiation beam pattern of the directional antenna can be thought of as a section of the omni-directional antenna beam pattern. Therefore, the directional antenna collects a portion of the total amount of multipath arrivals collected by an omni-directional antenna. This is shown in Figure 5.3 (b.1 and b.2) where signals arriving in the null section of the beam pattern are eliminated, and multipath cluster arrivals that exist are correlated in time with the squared magnitude response of the omni/omni antenna combination of Figure 5.3 (a.1 and a.2). Figure 5.3 (c.1 and c.2) shows a correlation amongst cluster arrivals with Figure 5.3 plots (a.1 and a.2), but there are less cluster arrivals due to the directional transmitter antenna.

A directional antenna employed at the transmitter has a greater effect on reducing initial cluster arrivals than a directional antenna employed at the receiver. This is shown in Figure 5.3 where the multipath has decreased considerably prior to 100 ns in plots c.1 and c.2 as compared to plots b.1 and b.2. On the other hand, it is observed that multipath arrivals proceeding 100 ns have not changed considerably when a directional antenna is used at the receiver with a directional transmitter. This results from the fact that the transmitter antenna is closer to the wall than the receiver antenna. When this is the case,

multipath components arriving from the back end of the receiver antenna travel a longer distance then the multipath components reflecting off the wall in close proximity to the transmitter. Therefore, when a directional antenna is employed at the receiver longer delayed arrivals are eliminated. On the other hand, when a directional transmitter antenna is used, the initial reflections reflecting off the wall in close proximity to the transmitter are eliminated due to the null point of the back end of the directional antenna. This indicates that a directional receiver antenna can considerably reduce longer delayed multipath arrivals, and a directional transmitter antenna can help reduce shorter delayed multipath arrivals in similar Tx/Rx scenarios.

5.3 Power Delay Profile Model

Figure 5.4 illustrates the average normalized power delay profiles of Figure 5.3 in a 2-dimensional view, where the vertical axis is linear and not in decibels. Note that the binned data is used in Figure 5.4, and not the raw data which was used in Figure 5.3. The PDP contains a relatively large first arrival signal starting at 0 ns as shown in Figure 5.4. Also, it is shown that the rays of the clusters tend to decay in an exponential nature. This corresponds to a linear decreasing function on a dB scale as shown in Figure 5.3. The first arrival component is relatively large, compared to subsequent multipath arrivals, causing clusters to appear greatly attenuated in the profile as compared to the first arrival signal. On the other hand, multipath components which appear greatly attenuated on a linear scale are greatly accentuated on a dB scale, indicating the significance of the clusters in the PDP as shown in Figure 5.3.

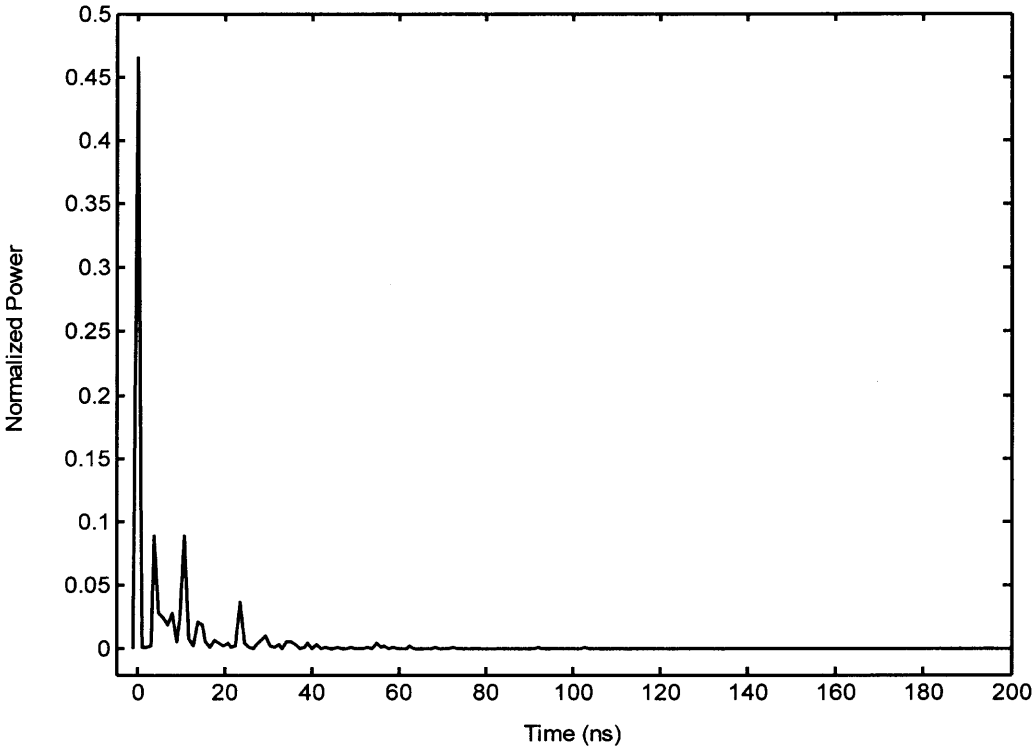

(a) omni-directional/omni-directional

Figure 5.4. Normalized power delay profile (measured) at a 4 m location in the classroom. (a) omni-directional/omni-directional. (b) omni-directional/directional. (c) directional/directional.

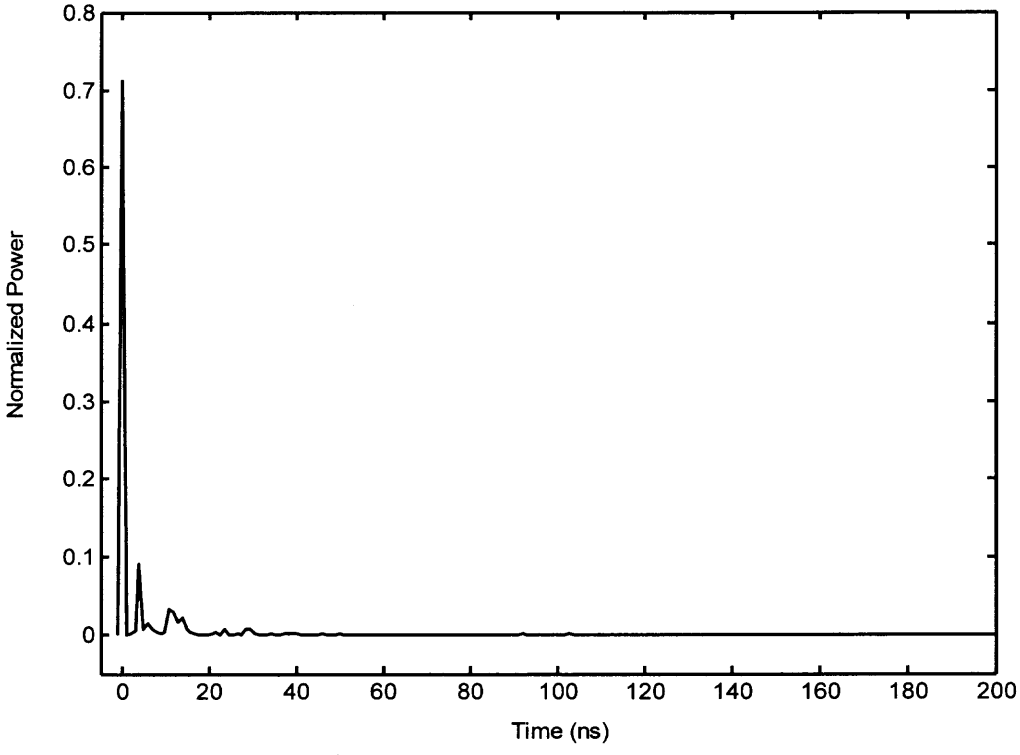

(b) omni-directional/directional

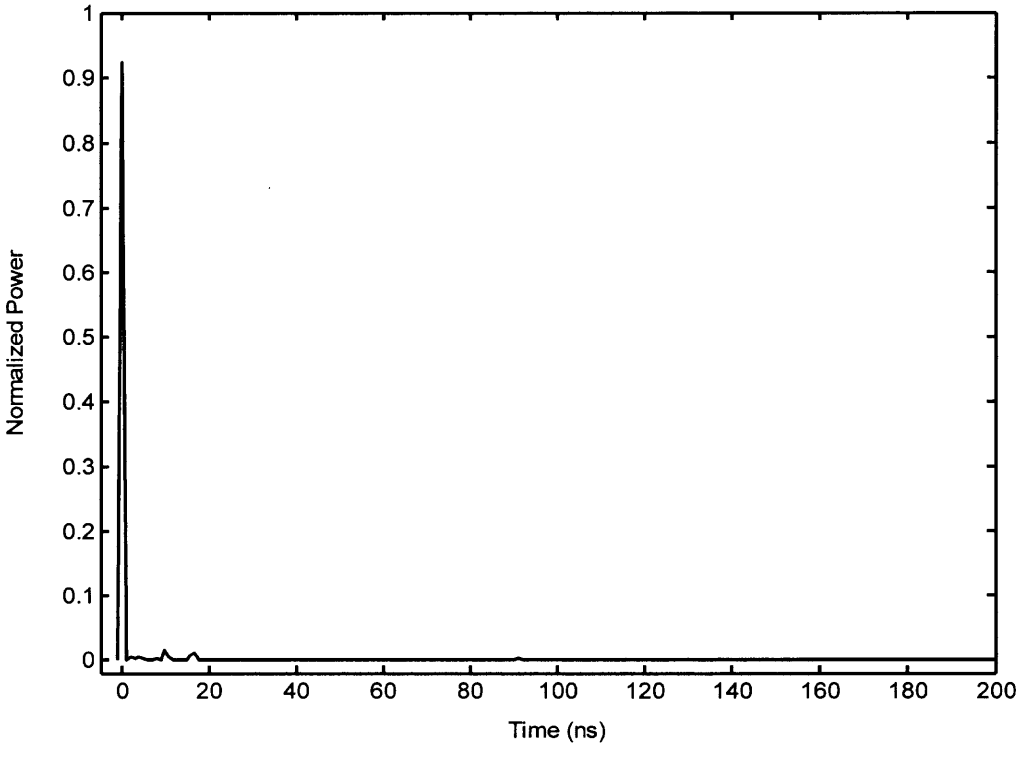

(b) directional/directional

Figure 5.4. (*Continued*)

Figure 5.5 is a zoomed-in version of the PDP's of Figure 5.4. This gives a more detailed visualization of the cluster arrivals and the exponential decaying nature inherent in the profiles.

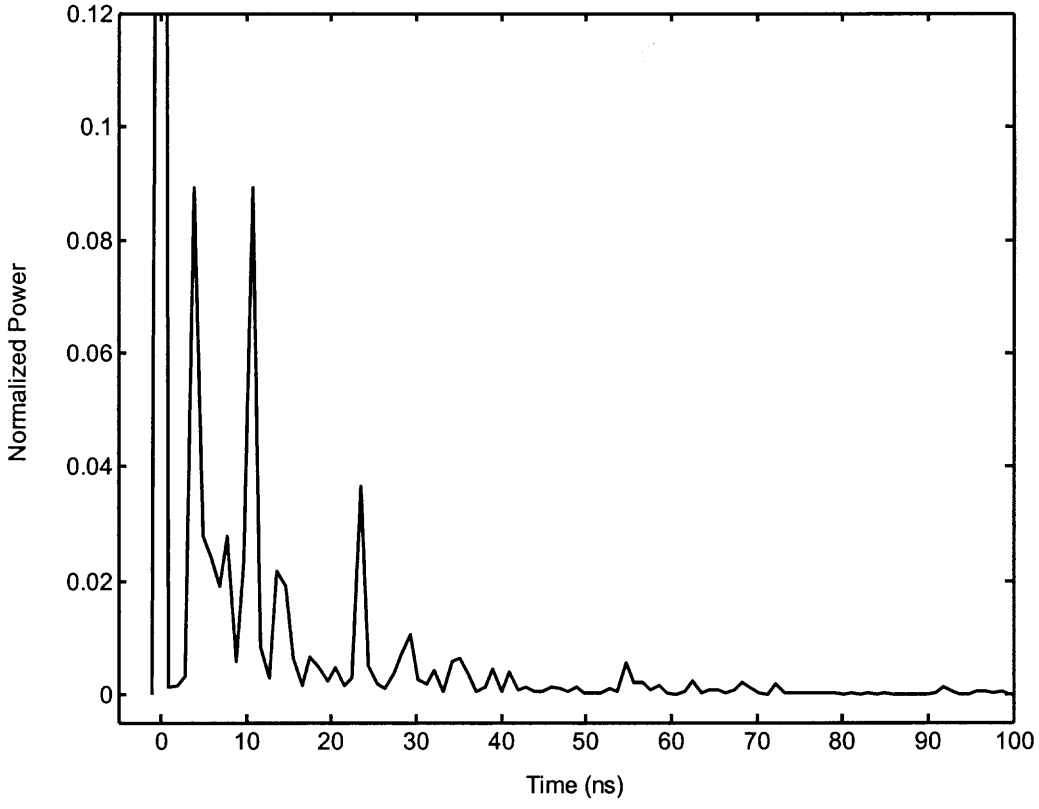

(a) omni-directional/omni-directional

Figure 5.5. Zoomed-in version of the normalized PDP's of Figure 5.4. (a) omni-directional/omni-directional. (b) omni-directional/directional.

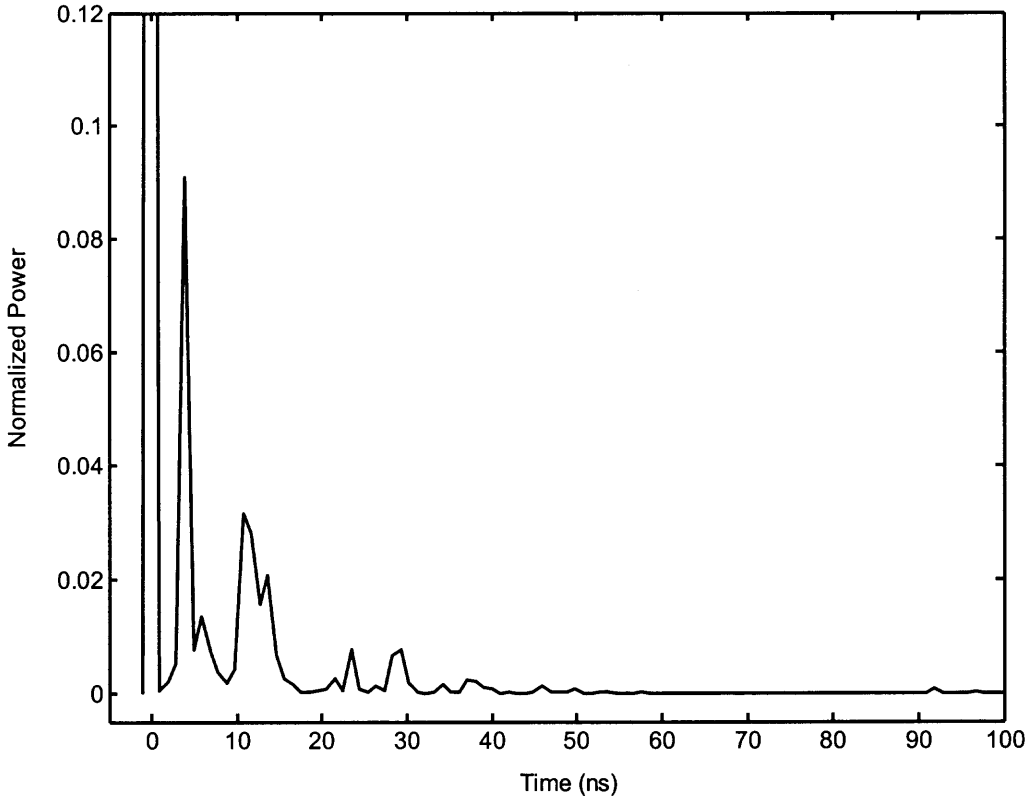

(b) omni-directional/directional

The PDP profile of the channel exhibits a large first arrival component, which can be represented as a delta function with unity gain by scaling the normalized PDP to its maximum component. This results in a PDP that is scaled relative to its maximum component, hence it is given the name *relative* PDP. Modeling the *relative* PDP of the channel has been shown to give significant results [13]. The *relative* PDP $P_{\text{rel}}(t;d)$ is given by:

$$P_{\text{rel}}(t;d) = \delta(t) + \sum_{l=0}^{L-1}\sum_{k=0}^{K-1}\beta_{kl}^2(d)\delta(t - \mathrm{T}_l - \tau_{kl} - \Delta\tau) \tag{5.9}$$

$P_{\text{rel}}(t;d)$ contains a unit gain component at $t = 0$ and a double summation term pertaining to the cluster and ray arrivals starting at $t = \Delta\tau$. Note that the double summation term used to represent the cluster and ray arrivals is given by the general representation of the Saleh-Valenzuela wideband channel model in [11], although in greater detail, differences arise in the characterization of β_{kl}.

5.4 Omni-Directional/Directional Channel Model Description

The general relative PDP model is given by Equation (5.9), and is dependent on the characterization of the arrival times T_l and τ_{kl}, and the power gains of the rays given by $\beta_{kl}^2(d)$. In this section a model is developed based on the characterization of these parameters.

The arrival time of the l^{th} cluster is denoted by T_l and the arrival time of the k^{th} ray of the l^{th} cluster is denoted by τ_{kl}. The first cluster starts at $T_0 = 0$ with respect to the initial time shift $\Delta\tau$ and the first ray of the l^{th} cluster starts at $\tau_{0l} = 0$. Therefore, τ_{kl} represents a vernier time shift adjustment within the l^{th} cluster. The interarrival times of the clusters, given by $\Delta T_l = T_l - T_{l-1}$ for $l > 0$, are exponentially distributed and thus are described by the probability density function,

$$p_X(x) = \Lambda e^{-\Lambda x}, \qquad x > 0 \tag{5.10}$$

where x corresponds to the interarrival times and Λ is the cluster arrival rate. The ray intra-arrival times are not exponentially distributed and are considered instead to be constant over all intra-arrival times of all clusters in which,

$$\tau_{kl} - \tau_{(k-1)l} = \tau_{mn} - \tau_{(m-1)n}, \qquad \forall \begin{Bmatrix} k,m > 0 \\ l,n \geq 0 \end{Bmatrix} \tag{5.11}$$

A double exponential model is used in [11] to characterize the mean square values of the impulse response of the channel. Similar channel behavior characteristics are experienced for measurements described in this thesis and thus a modified double exponential model is used to characterize the median power gains $\left\{\widehat{\beta_{kl}^2}(d)\right\}$ estimated via least-squares fitting to the logarithmic data of the $\left\{\beta_{kl}^2(d)\right\}$ path gains of Eq. (5.9). The multipath in the channel increases as a function of distance as described in Chapter 4 through RMS delay spread analysis. Therefore, $\beta_{kl}^2(d)$ which represents the path gain of the k^{th} multipath component of the l^{th} cluster is modeled as a function of distance. The median power gains $\left\{\widehat{\beta_{kl}^2}(d)\right\}$ are given by,

$$\widehat{\beta_{kl}^2}(d) = \widehat{\beta_{00}^2}(d) e^{-\frac{T_l}{\Gamma(d)}} e^{-\frac{\tau_{kl}}{\gamma_p}}, \qquad k \geq 0, l \geq 0 \tag{5.12}$$

where $\Gamma(d)$ is the cluster decay factor, or rather the cluster decay time constant, described by a probability distribution with a mean that changes over distance; γ_p is the ray decay factor, where the first cluster is associated with a different decay factor than subsequent clusters; and $\widehat{\beta_{00}^2}(d)$ is a median estimate of the power gain of the first multipath component of the first cluster. The power gains $\beta_{kl}^2(d)$ are independent positive random variables given by,

$$\beta_{kl}^2(d) = \begin{cases} \widehat{\beta_{kl}^2}(d) \cdot \Psi_l, & \text{for } k = 0, l \geq 0 \\ \widehat{\beta_{kl}^2}(d) \cdot \xi_{kl}, & \text{for } k > 0, l \geq 0 \end{cases} \tag{5.13}$$

where ξ_{kl} is a random variable describing the random variation of the k^{th} ray of the l^{th} cluster for $k > 0$ and Ψ_l describes the random variation of the first ray (i.e, $k = 0$) of the l^{th} cluster. Therefore, $P_{\text{rel}}(t;d)$ of Eq. (5.9) can be represented as,

$$P_{\text{rel}}(t;d) = \delta(t) + \sum_{l=0}^{L-1}\sum_{k=0}^{K-1} \widehat{\beta_{00}^2}(d) e^{-\frac{T_l}{\Gamma(d)}} e^{-\frac{\tau_{kl}}{\gamma}} \xi_{(k\neq 0)l} \Psi_l \delta(t - T_l - \tau_{kl} - \Delta\tau). \quad (5.14)$$

The normalized PDP P_{norm} of Eq. (5.7) can be realized by normalizing $P_{\text{rel}}(t;d)$ of Eq. (5.14) [13] and is given by,

$$P_{\text{norm}}(t;d) = \left(\sum_{i=0}^{N-1} P_{\text{rel}}(t_i;d) \right)^{-1} \cdot P_{\text{rel}}(t;d). \quad (5.15)$$

Equations (5.14) and (5.15) completely characterize the normalized PDP of the channel at any given distance, (e.g., between 1 m and 10 m for the measured channel described in this thesis).

5.5 Omni-Directional /Directional Channel Model Parameters

As mentioned previously, the PDP of the channel consists of a large first arrival signal (e.g. LOS component). Furthermore, subsequent multipath components arrive in clusters that decay in an exponential nature and rays within the clusters which also decay exponentially. The channel model representing this phenomenon is given by Equation (5.14). The channel model given by Equation (5.14) can be represented in linear form by taking the logarithm of the function. This enables linear regression techniques to be used for extracting the given parameters of Equation (5.14). The linear transformation of Equation (5.14) in dB is given by,

$$P_{\text{rel}}(t;d)_{\text{dB}} = \begin{cases} 0 & \text{for } t = 0 \\ \left[\widehat{\beta_{00}^2}(d)_{\text{dB}} - \left(\dfrac{10\cdot \text{T}_l}{\ln(10)\cdot\Gamma(d)}\right) - \dfrac{10\cdot\tau_{kl}}{\ln(10)\cdot\gamma} + \xi_{(k\neq 0)l}(\text{dB}) \right. \\ \left. +\Psi_l(\text{dB})\right]\delta(t-\text{T}_l-\tau_{kl}-\Delta\tau) & \text{for } t>0 \;\&\; k\geq 0,\, l\geq 0 \end{cases} \tag{5.16}$$

5.5.1 Cluster Intercept Parameter

The mean power gain of the first component of the first cluster is denoted by $\widehat{\beta_{00}^2}(d)_{\text{dB}}$, which represents a minimum mean square error (MMSE) estimate of the power of the first ray of the first cluster at a given distance *d*. Therefore, the cluster intercept estimates (e.g., MMSE estimate of the power of the first ray of the first cluster) obtained from fitting a line to the cluster data in the mean square error sense are plotted versus distance. This parameter is modeled as a random variable with a mean that increases as a function of distance. When the receiver is positioned at a distance close to the transmitter (e.g., 1 m to 3 m), multipath components are highly attenuated by the antenna side lobes. As the receiver is positioned farther away from the transmitter, multipath components are more prone to arriving within the maximum gain region of the antenna resulting in multipath signals which are less attenuated with respect to the first arrival component. Therefore, at a close distance or, more specifically at 1 m, the total power of the PDP is mostly contained in the first arrival component.

The MMSE estimate $\widehat{\beta_{00}^2}(d)_{\text{dB}}$ in dB is given by,

$$\widehat{\beta_{00}^2}(d)_{\text{dB}} = \frac{10\cdot\ln[\widehat{\beta_{00}^2}(d)]}{\ln(10)} = 10\cdot\log_{10}[\widehat{\beta_{00}^2}(d)], \tag{5.17}$$

and is modeled as,

$$\widehat{\beta_{00}^2}(d)_{\mathrm{dB}} = \left(\widehat{\mathrm{B}^2} + \varepsilon \cdot 10 \cdot \log_{10}(d)\right) + \eta, \tag{5.18}$$

where $\widehat{\mathrm{B}^2}$ is the MMSE estimate of all cluster intercept MMSE estimates at 1 m, ε is the slope of the MMSE fitted line in dB/m, d is the Tx/Rx separation distance in meters, η is a zero mean Guassian random variable with a standard deviation of σ_η, which is the standard deviation of the residuals or rather the differences between the observations and the fitted line. η is given by,

$$\eta = \eta_0 \sigma_\eta, \tag{5.19}$$

where η_0 is a zero mean Guassian random variable with unit variance. Figure 5.6 is a plot of the cluster intercept MMSE estimates versus distance along with the least squares fit to the data. Figure 5.7 is a normal probability plot of the residuals of the least squares fit to the data in Figure 5.6. The values of the model parameters of Equation (5.18) corresponding to Figures 5.6 and 5.7 are shown in Table 5.1.

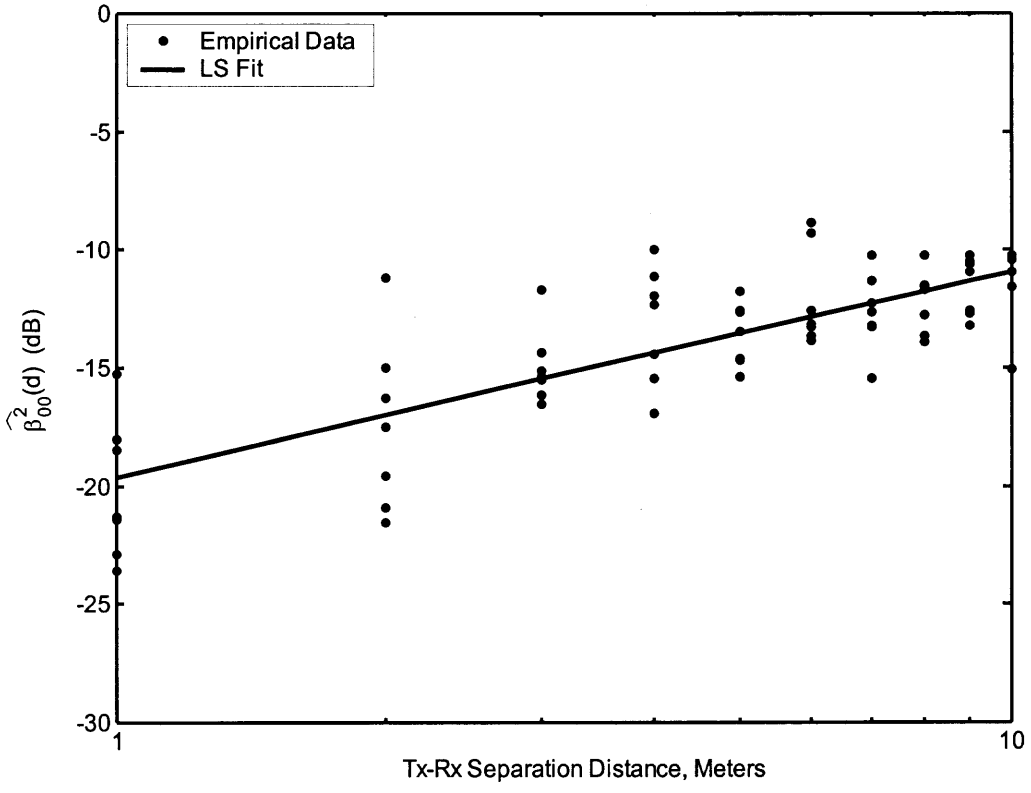

Figure 5.6. Cluster intercept MMSE estimates versus distance for the omni-directional/directional Tx/Rx antenna combination.

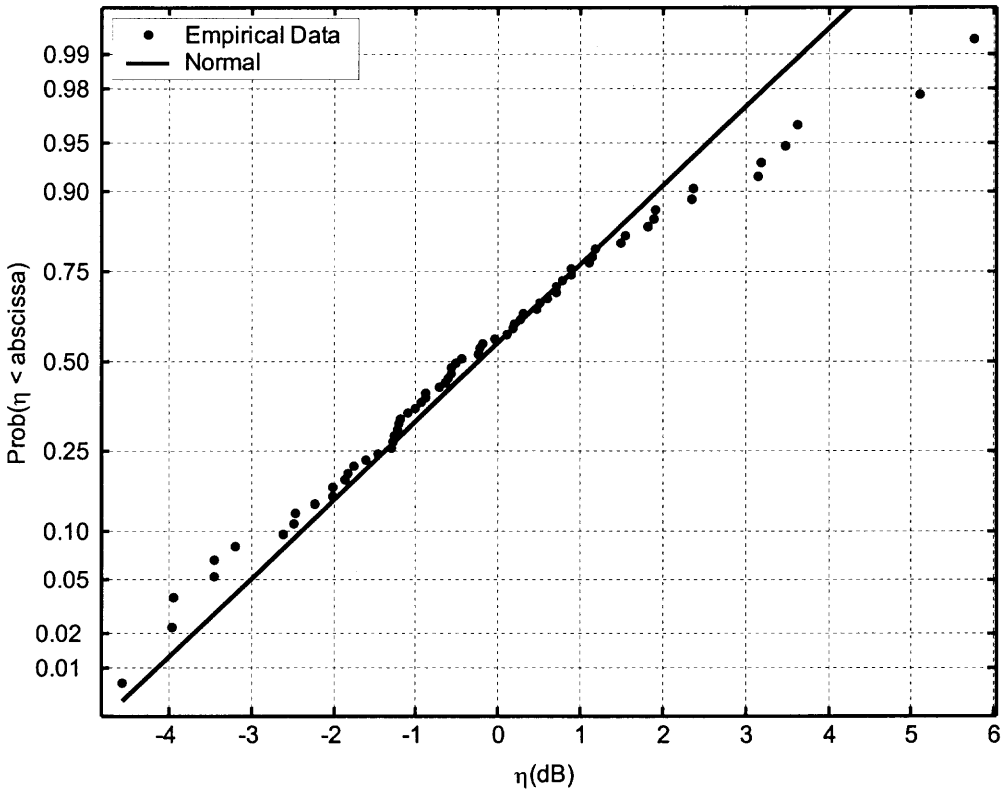

Figure 5.7. Residuals of the least squares fit to the MMSE cluster intercept estimates of Figure 5.6.

Table 5.1. MMSE Estimates for Parameters of Equation (5.18)

Parameter	Estimated Value
$\widehat{B^2}$	-19.6 dB
ε	.87
σ_η	2.1 dB

5.5.2 Cluster Interarrival and Ray Intra-arrival Times

As explained in Section 5.4, the cluster interarrival times are exponentially distributed and modeled using Equation (5.10). The mean interarrival time is given by $1/\Lambda$ and is estimated to be approximately 20 ns. Figure 5.8 is a quantile-quantile plot of the cluster interarrival times of the empirical data versus theoretical exponentially distributed interarrival time samples with parameter $\Lambda = (20\,\text{ns})^{-1}$. As shown in the figure, the interarrival times of the clusters fit the theoretical line reasonably well indicating that the exponential distribution is a valid model for the cluster interarrival times. The rays within the clusters do not exhibit any distribution amongst the intra-arrivals and are considered to arrive constantly with an intra-arrival time $\Delta\tau = .9768\,\text{ns}$. This value corresponds to the bin time of each multipath component, as explained in Chapter 4.

5.5.3 Cluster and Ray Decay Factors

The cluster decay factor is an MMSE estimate corresponding to the slope of the least-squares fit to the cluster data in dB. The decay factors are averaged at each distance d and then a least squares regression model is fitted to the data. The cluster decay factor $\Gamma(d)$ is modeled as a function of distance and is given by,

$$\Gamma(d) = \Gamma_0 + \upsilon \cdot 10\log_{10}(d), \tag{5.20}$$

where Γ_0 is an MMSE estimate of the cluster decay factor at a distance of 1 m, d is the aforementioned Tx/Rx separation distance, and υ is an MMSE estimate of the slope of the least squares fit to the data. Therefore, there is single value representing the cluster decay factor at each distance d. It is intuitive that the cluster decay factor is conducive to or rather contributes to the increase in RMS delay spread experienced over distance.

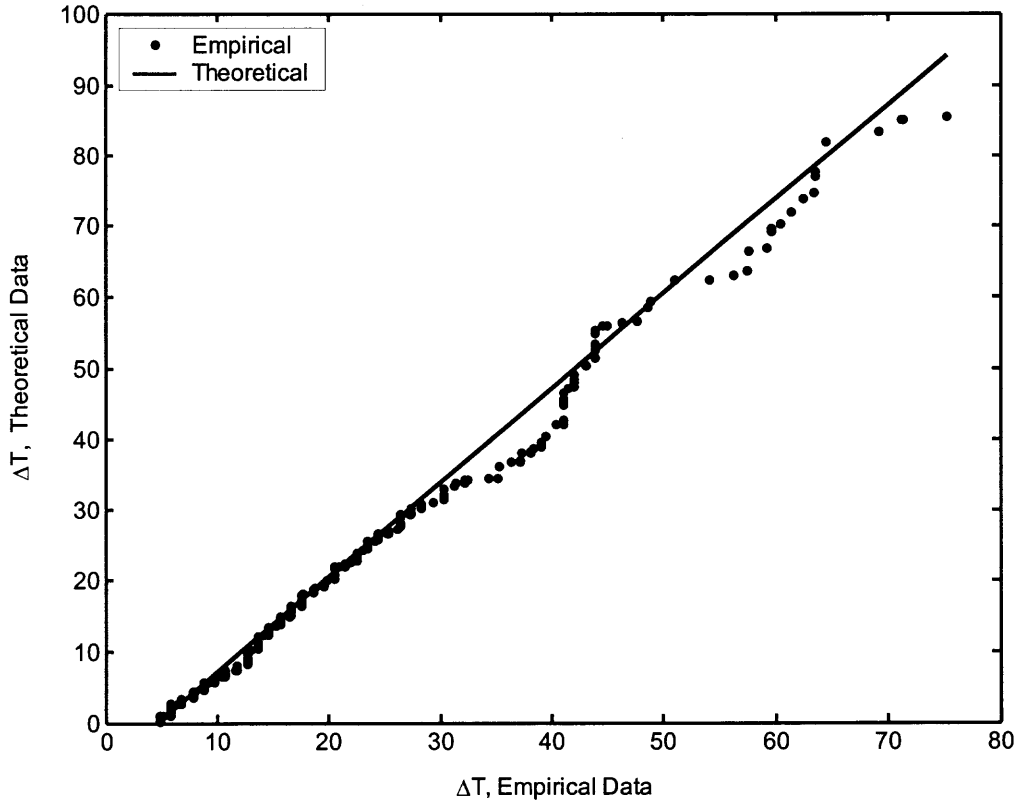

Figure 5.8. Quantile-Quantile plot of the cluster interarrival times versus exponentially distributed random samples with parameter $\Lambda = (20\,\text{ns})^{-1}$.

Figure 5.9 represents the average cluster decay factors plotted versus distance along with the least squares fit to the data. Note the increasing trend of the cluster decay factor with distance, corresponding to a relative increase in RMS delay spread over distance. Table 5.2 lists the parameter values of Equation (5.20), representing the least squares fit to the data of Figure 5.9. The ray decay factor γ, or rather the decay time constants of the clusters, did not exhibit any trend over distance. On the other hand, it appears that the first set of rays corresponding to the first cluster decay at a greater rate then subsequent clusters of rays on the average. The mean decay time constant of the first cluster has a

decay time constant denoted by γ_1 and subsequent clusters correspond to a decay time constant denoted by γ_2. The data-derived values of γ_1 and γ_2 are 3 ns and 5 ns, respectively.

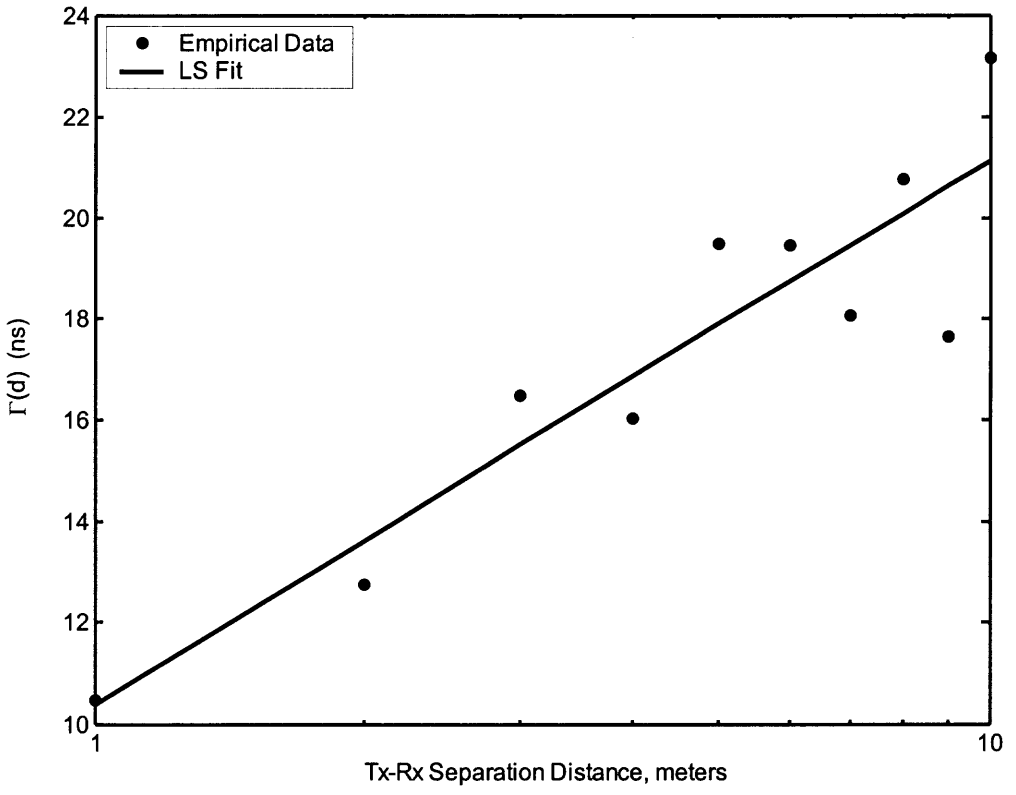

Figure 5.9. Average cluster decay factors versus Tx/Rx separation distance.

Table 5.2 MMSE Estimates for Parameters of Equation (5.20)

Parameter	Estimated Value
Γ_0	10.4 ns
υ	1.07 ns/dB

5.5.4 Random Variation of Cluster and Ray Power Gains

The dB power gains of the rays and clusters are zero mean Guassian distributed random variables with differing standard deviations. It has been deduced from analyzing cluster arrivals and tracing propagation paths of PDPs, that the floor and surrounding walls within a room are contributing factors of cluster arrivals. On the other hand, the rays within the clusters were deduced to be a result of the clutter present in the environment. This has also been observed in [11].

The median response of the channel is given by Equation (5.12), and the random variation of the rays and clusters about the median response in dB are described by $\xi(\text{dB})$ and $\Psi(\text{dB})$, respectively. Equation (5.13) in dB is given by,

$$\beta_{kl}^2(d)_{\text{dB}} = \begin{cases} \widehat{\beta_{kl}^2}(d)_{\text{dB}} + \Psi_l(\text{dB}), & \text{for } k = 0, l \geq 0 \\ \widehat{\beta_{kl}^2}(d)_{\text{dB}} + \xi_{kl}(\text{dB}), & \text{for } k > 0, l \geq 0 \end{cases} \tag{5.21}$$

$\Psi(\text{dB})$ and $\xi(\text{dB})$ are zero mean Guassian distributed random variables in dB as shown in Figure 5.10 and Figure 5.11, respectively. The standard deviations of $\Psi(\text{dB})$ and $\xi(\text{dB})$ are denoted by σ_Ψ and σ_ξ, respectively, and are listed in Table 5.3.

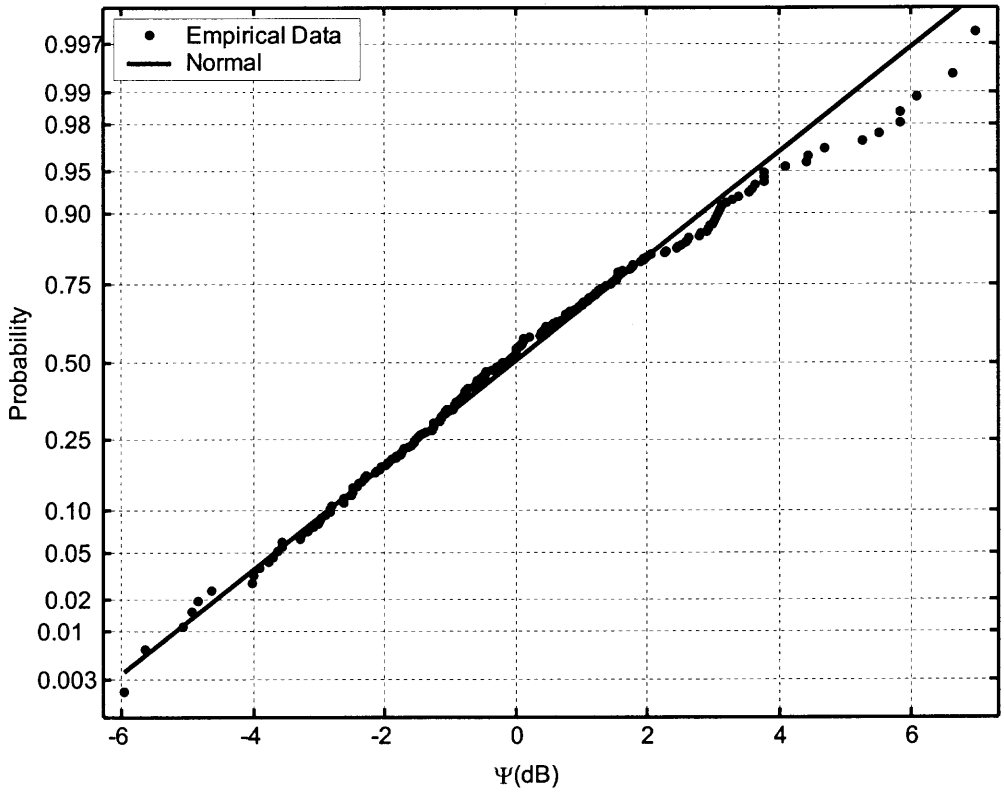

Figure 5.10. Distribution of cluster power gains about the mean response in dB.

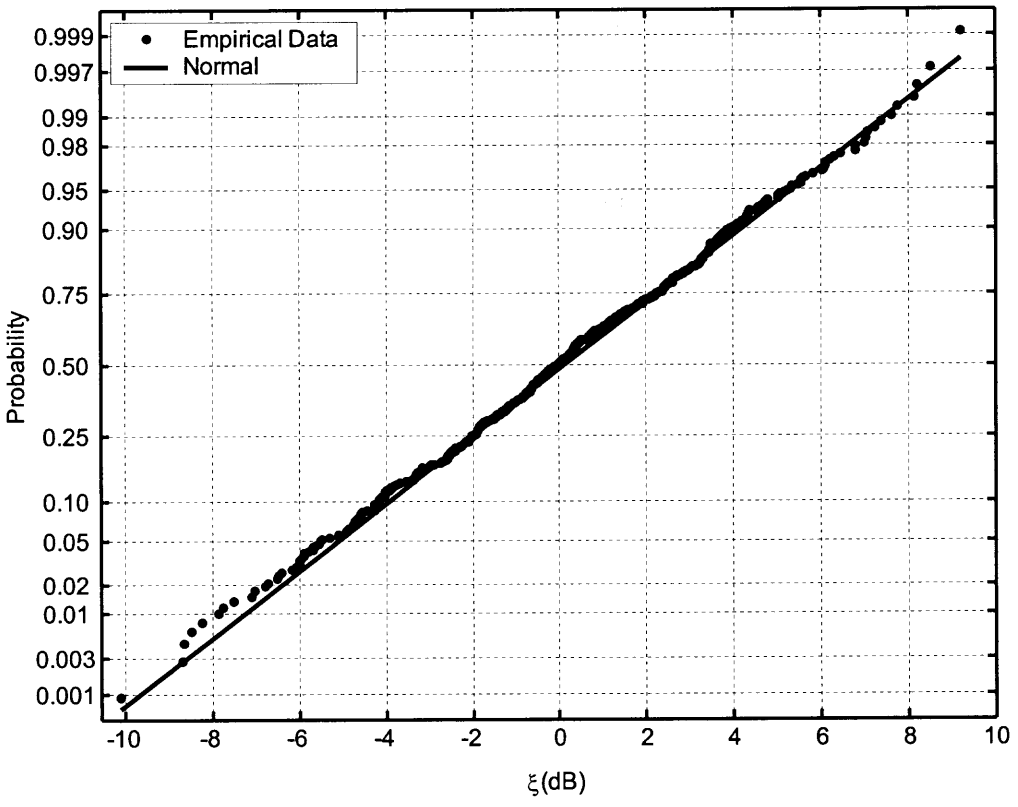

Figure 5.11. Distribution of ray power gains about the mean response in dB.

Table 5.3. Standard Deviations of Cluster and Ray Power Gain Distributions

Parameter	Estimated Value
σ_{Ψ}	2.3 dB
σ_{ξ}	3.2 dB

5.6 Omni-Directional/Directional Channel Model Simulation Results

The relative PDP given by Equation (5.16) can be synthesized using the parameter estimates described in Section 5.5. The normalized PDP of Equation (5.7) can be realized by transforming the synthesized response to a linear scale and using Equation (5.15) to normalize the relative PDP. The phase term θ in Equation (5.7) is described as a uniform random variable over $[0, 2\pi)$. Note that the first arrival component is always positive (i.e., $\theta = 0$).

The clusters of the relative PDP model are generated for $T_l < 130\,\text{ns}$ to ensure ray arrivals are simulated up to and beyond the average maximum multipath excess delay of approximately 120 ns. The ray arrivals are simulated for $\tau_{kl} < 8 \cdot \gamma_p$ where $p = 1$ denotes the first cluster decay factor and $p = 2$ denotes the decay factor of subsequent clusters. This corresponds to ray delays up to 40 ns beyond the cluster delay T_l. After normalization of the relative PDP all power gains falling below a threshold of 45 dB are set to zero. This corresponds to the average noise level of the measured data.

RMS delay spread is a feasible parameter for testing the significance or validity of the channel model and how well it reproduces the characteristics of the measured data. As shown in Chapter 4, the RMS delay spread increases as a function of distance, and the model should indeed capture this effect. Figure 5.12 is a scatter plot of RMS delay spread versus distance corresponding to seven simulated PDPs per distance. As shown in the plot, the model captures the effect of the RMS delay spread increasing over distance. The least squares fit to the simulated data and the least squares fit to the measured data are also shown in Figure 5.12. Note that in this particular trial run the least squares fit to the simulated data is approximately identical to the least squares fit of the measured data.

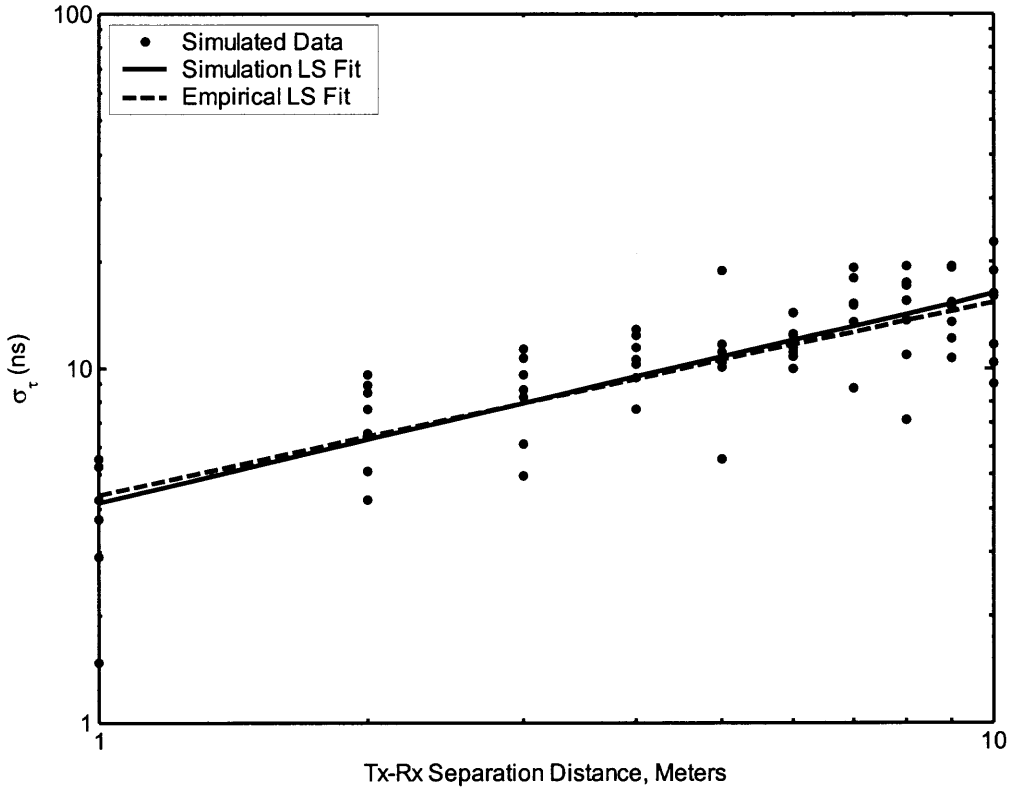

Figure 5.12. RMS delay spread vs. distance computed from simulated data. The solid line represents the least squares fit to the simulated data, and the dashed line corresponds to the least squares fit to the RMS delay spread values of the measured data.

A CDF plot of RMS delay spread values computed from simulated data is shown in Figure 5.13, along with the CDF of the RMS delay spread values of the measured data. It is shown that the model reproduces a CDF plot similar to that of the empirical CDF plot, confirming the validity of the model.

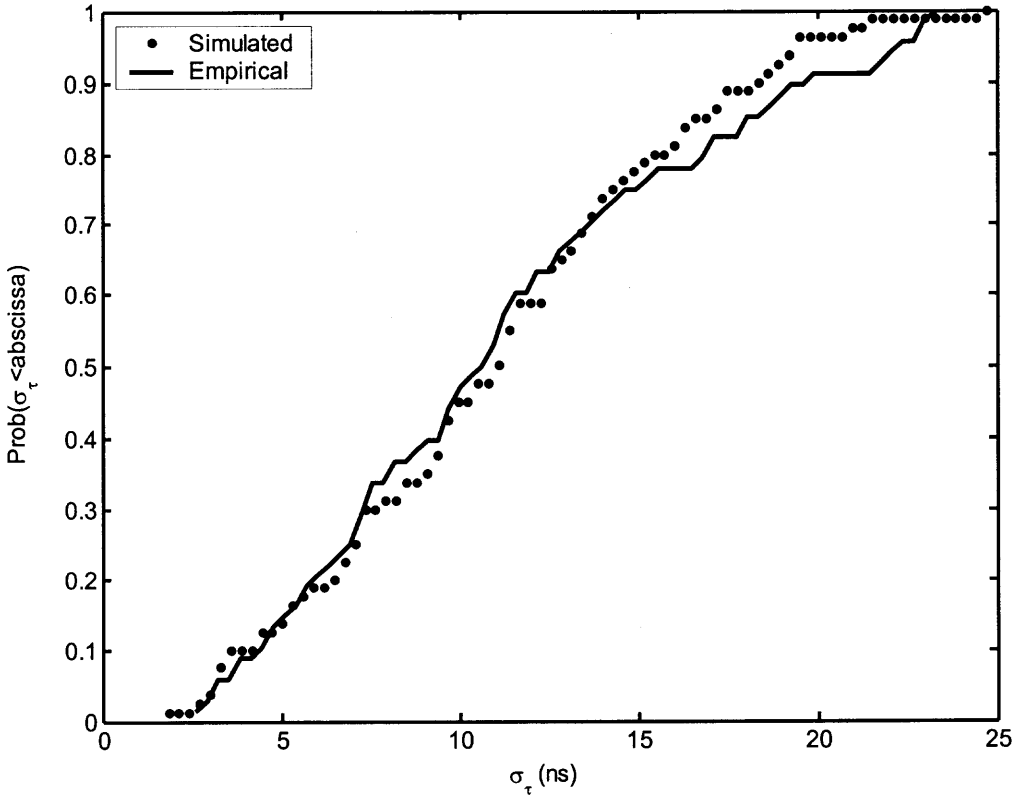

Figure 5.13. RMS delay spread CDF plots computed from simulated and empirical data.

A simulated normalized PDP representing a 4 m response is shown in Figure 5.14a. This closely matches the 4 m PDP response of Figure 5.4b, which is shown in Figure 5.14b for convenience. Figure 5.15a illustrates an 8 m simulated PDP response and Figure 5.15b is a measured 8 m PDP response, note the similarities amongst these two figures. It is exemplified in Figures 5.14 and 5.15 that the model of Equation (5.16) reproduces PDP responses of the channel exhibiting channel characteristics similar to those of the measured data.

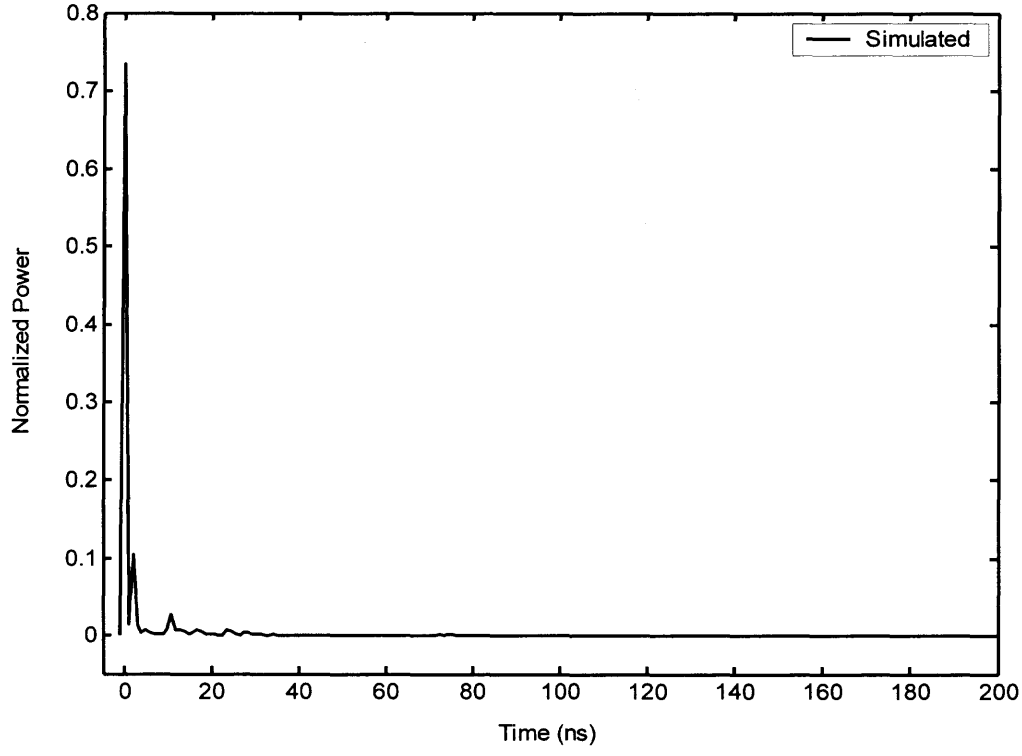

(a)

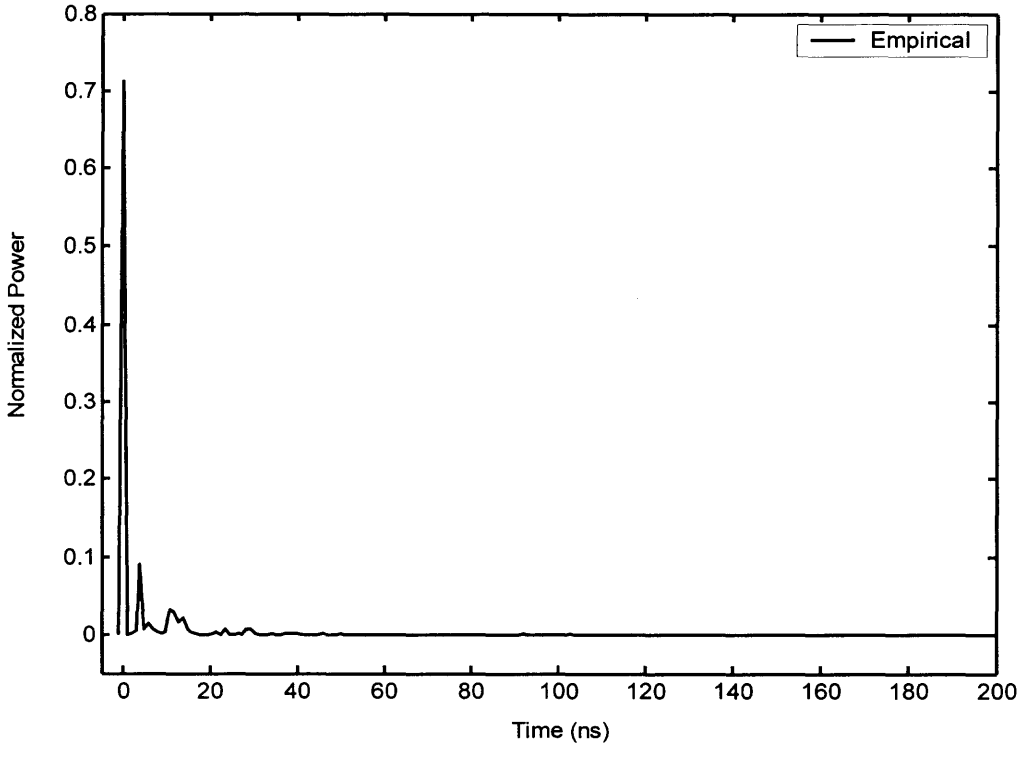

(b)

Figure 5.14. 4 m normalized PDP response. (a) Simulated. (b) Empirical.

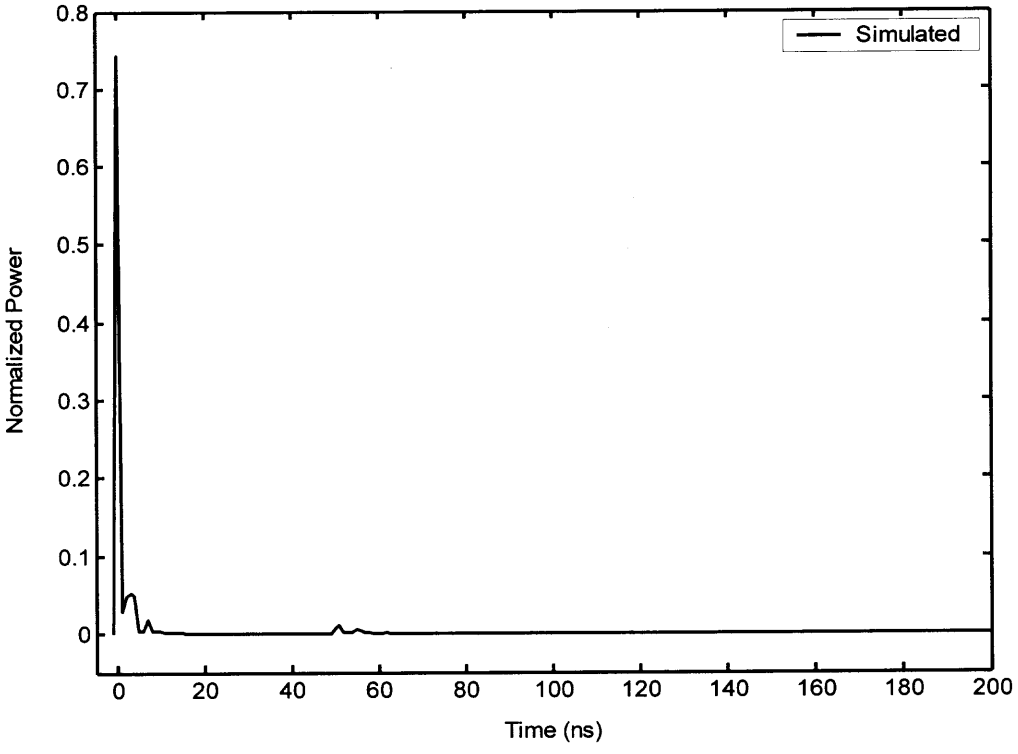

(a)

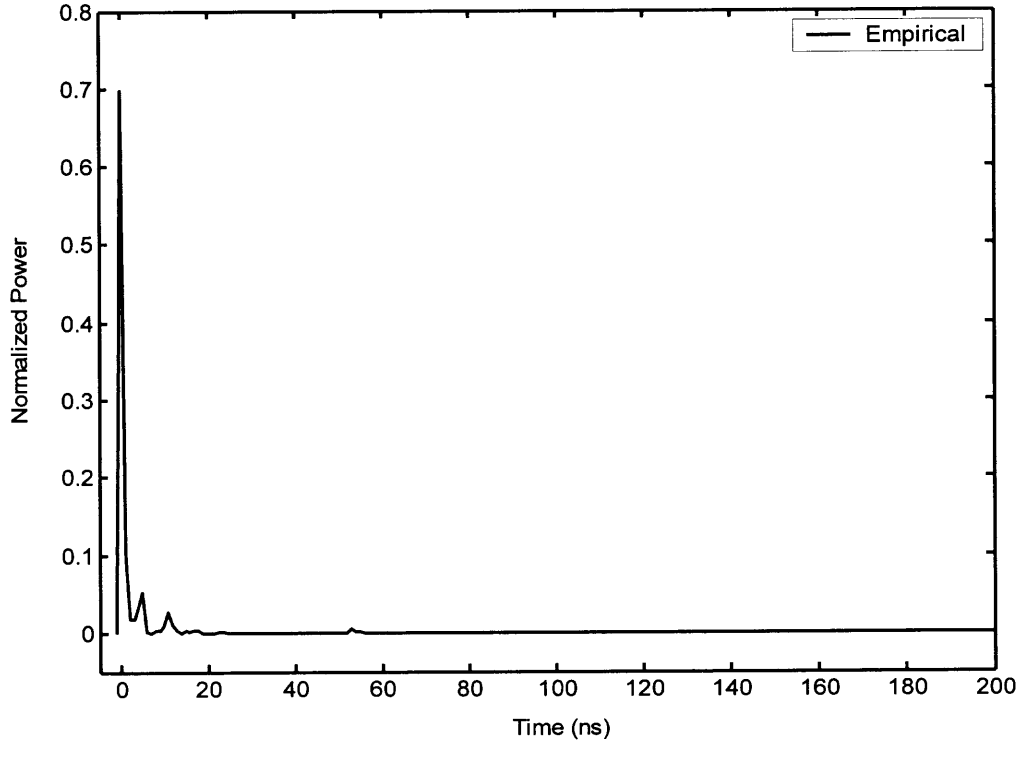

(b)

Figure 5.15. 8 m normalized PDP response. (a) Simulated. (b) Empirical.

The simulation model data was also analyzed for threshold levels of 10 dB, 20 dB, and 30 dB below the maximum component of the normalized PDP response. That is, the number of paths and the mean RMS delay spread were computed for each threshold level and are listed in Table 5.4.

Table 5.4. Mean Values of σ_τ and Number of Paths N_p of Simulated Data for Threshold Levels of 10 dB, 20 dB, and 30 dB Below the Maximum Component

Threshold	$\overline{\sigma}_\tau$	$\overline{N}_p$
10 dB	1 ns	2
20 dB	5.6 ns	13
30 dB	9.5 ns	40

Comparing the values of Table 5.4 with those of Table 4.3, it is evident that the simulation model is highly reliable and accurate for threshold levels of 10 dB and 20 dB. For a 30 dB threshold the model actually is highly reliable even though it lacks 8 paths with regard to the measured data. This is true since the eight paths have been determined to exist approximately at the 30 dB threshold level in which a 2 dB gain over the given threshold level results in exactly 40 paths. Moreover, there was no significant change in the mean RMS delay spread value for this threshold. Therefore, it can be concluded that these paths do not carry significant energy at this threshold level, and for all practical purposes the simulation model is valid at the 30 dB threshold.

5.7 Summary

In this chapter, the impulse response of the channel was thoroughly investigated for three antenna combinations. Results show that the channel consists of a large first arrival signal and rays that arrive in clusters. PDP plots for each antenna combination were shown in 2-dimensional and 3-dimensional views, illustrating the effect of antenna directivity on multipath propagation. It has been concluded that directional antennas employed at the receiver or transmitter can help reduce multipath excess delay in the channel.

A general representation of the impulse response model is described, which can be modeled as a combination of the path loss model and normalized PDP model. A distant-dependent relative PDP model of the channel is proposed which consists of a delta function representing the LOS component and a double exponential model representing the clustering phenomenon of rays. This simulation model is characterized for an omni-directional/directional antenna combination and shows favorable agreement with the measured data. The model can be used to regenerate impulse responses of the channel for any location at any given distance from 1 m to 10 m for an environment with homogeneous characteristics to the measured environment explained in Chapter 2. Results show that the model reproduces statistical characteristics of the measured channel with high accuracy.

CHAPTER 6

CONCLUSIONS

Frequency domain measurements of the indoor UWB channel were performed in a college campus building for three different Tx/Rx antenna combinations using omni-directional and directional antennas. The measurement procedure, environment, data processing and statistical analysis of the channel are described. A statistical model that characterizes the path loss in the channel was developed from the empirical data measured in the channel for all three antenna combinations. This model can be used for predicting the attenuation in the indoor UWB channel as a function of distance. Statistics of the shadow fading in the environment are shown to be log-normally distributed.

Statistical analysis in the temporal domain was achieved by transforming the frequency domain data into the time domain using the IDFT. The RMS delay spread has been shown to decrease considerably when using directional antennas as opposed to using omni-directional antennas. Therefore, directional antennas can be used to mitigate the effects of multipath in the indoor UWB channel that occur for omni-directional antennas (e.g., transmission errors).

The RMS delay spread was shown to increase as a function of distance for all three antenna combinations. Although, over distance RMS delay spread was shown to be more sensitive to directional antennas than omni-directional antennas. This in effect results in the ability to achieve higher data rates when the transmitter and receiver are within close proximity of each other (e.g. 1 m-3 m) as compared to a Tx/Rx separation distance of 10 m. The RMS delay spread was shown to increase at the lowest rate over

distance when using an omni-directional Tx/Rx antenna combination. The mean RMS delay spread and mean number of paths were computed for threshold levels of 10 dB, 20 dB, and 30 dB below the main peak for all three antenna combinations. Directional antennas were shown to considerably reduce the number of paths and delay spread over the given threshold levels with significant results for a 30 dB threshold level. Results show that a 30 dB threshold level gathers most of the energy in the PDP for each antenna combination correspondingly and thus can be considered a suitable threshold level for all three antenna combinations.

The deviation in RMS delay spread over distance was shown to be log-normally distributed. Furthermore, large deviations of RMS delay spread tend to be correlated with larger path loss values at a given distance for the omni/omni and omni/dir antenna combinations. On the other hand, the dir/dir antenna combination did not exhibit much correlation, and thus the RMS delay spread and shadow fading for this antenna combination can be considered uncorrelated.

The channel impulse response was analyzed and characterized through physical explanations and mathematical modeling. It was visually shown that directional antennas employed at the receiver can significantly reduce longer delayed multipath components. On the other hand, employing a directional antenna at the transmitter has been shown to significantly reduce shorter delayed multipath components in the channel. These findings are based on the transmitter antenna being set up in closer proximity to the wall than the receiver antenna. The channel consists of a large LOS component and multiple signals arriving from multiple propagation paths as a result of the clutter and walls of the indoor environment. The multipath in the channel appears to arrive in clusters which decay in

an exponential nature and rays within the clusters which also decay in an exponential nature. This phenomenon has been observed for wideband indoor measurements in [11], and thus a modified channel model based on the approach in [11] has been proposed. The proposed channel model is a distant-dependent impulse response model of the UWB channel for LOS indoor environments. Simulation results (i.e., RMS delay spread and PDPs) for the omni/dir antenna combination were shown to significantly agree with the measured data.

REFERENCES

[1] Federal Communications Commission, "Revision of Part 15 of the Commission's Rules Regarding Ultra-Wideband Transmission Systems. First Report and Order," *ET Docket 98-153, FCC 02-48*, pp. 1-118, Feb. 14, 2002.

[2] D.M.J. Devasirvatham, "Time Delay Spread and Signal Level Measurements of 850 MHz Radio Waves in Building Environments," *IEEE Trans. Antennas Propagat.*, vol. 34, pp. 1300-1305, Nov. 1986.

[3] D.M.J. Devasirvatham, "Multipath Time Delay Spread in the Digital Portable Radio Environment," *IEEE Commun. Mag.*, vol. 25, pp. 13-21, June 1987.

[4] D.M.J. Devasirvatham, "Time Delay Spread Measurements at 850 MHz and 1.7 GHz Inside a Metropolitan Office Building," *IEEE Electron. Lett.*, vol. 25, pp. 194-196, Feb. 1989.

[5] D.M.J. Devasirvatham, "Radio Propagation Measurements at 850 MHz, 1.7 GHz and 4 GHz Inside Two Dissimilar Office Buildings," *IEEE Electron. Lett.*, vol. 26, pp. 445-447, Mar. 1990.

[6] H. Hashemi, "Impulse Response Modeling of Indoor Radio Propagation Channels," *IEEE J. Select. Areas Commun.*, vol. 11, pp. 967-978, Sept. 1993.

[7] S.J. Howard and K. Pahlavan, "Measurement and Analysis of the Indoor Radio Channel in the Frequency Domain," *IEEE Trans. Instrum. Measure.*, vol. 39, pp. 751-755, Oct. 1990.

[8] T.S. Rappaport, "Characterization of UHF Multipath Radio Channels in Factory Buildings," *IEEE Trans. Antennas Propagat.*, vol. 37, pp. 1058-1069, Aug. 1989.

[9] T.S. Rappaport and D.A. Hawbaker, "Wide-Band Microwave Propagation Parameters Using Circular and Linear Polarized Antennas for Indoor Wireless Channels," *IEEE Trans. Commun.*, vol. 40, pp. 240-245, Feb. 1992.

[10] C.M.P. Ho and T.S. Rappaport, "Effects of Antenna Polarization and Beam Pattern on Multipath Delay Spread and Path Loss in Indoor Obstructed Wireless Channels," in *Proc. IEEE Int. Conf. Universal Personal Commun.*, pp. 04.02.1-04.02.5., 1992.

[11] A.A.M. Saleh and R.A. Valenzuela, "A Statistical Model for Indoor Multipath Propagation," *IEEE J. Select. Areas Commun.*, vol. SAC-5, pp. 128-137, Feb. 1987.

[12] S.S. Ghassemzadeh, R. Jana, C.W. Rice, W. Turin, and V. Tarokh, "A Statistical Path Loss Model For In-Home UWB Channels," in *Proc. IEEE Conf. Ultra Wideband Systems and Technol.*, pp. 59-64, May 2002.

[13] S.S. Ghassemzadeh, L.J. Greenstein, T. Sveinsson, and V. Tarokh, "A Multipath Intensity Profile Model For Residential Environments," in *Proc. IEEE Conf. Wireless Commun. and Networking*, pp. 150-155, Mar. 2003.

[14] M.Z. Win, R.A. Scholtz, and M.A. Barnes, "Ultra-Wide Bandwidth Signal Propagation for Indoor Wireless Communications," in *Proc. IEEE Int. Conf. Commun.*, pp. 56-60, June 1997.

[15] M.Z. Win and R.A. Scholtz, "On the Robustness of Ultra-Wide Bandwidth Signals in Dense Multipath Environments," *IEEE Commun. Lett.*, vol. 2, pp. 10-12, Feb. 1998.

[16] D. Cassioli, M.Z. Win, and A.F. Molisch, "A Statistical Model for the UWB Indoor Channel," in *Proc. IEEE Conf. on Veh. Technol.*, vol. 2, pp. 1159-1163, May 2001.

[17] D. Cassioli, M.Z. Win, and A.F. Molisch, "The Ultra-Wide Bandwidth Indoor Channel: From Statistical Model to Simulations," *IEEE J. Select. Areas Commun.*, vol. 20, pp. 1247-1257, Aug. 2002.

[18] J. Foerster, "Channel Modeling Sub-committee Report Final," IEEE P802.15 Working Group for Wireless Personal Area Networks. (Feb. 7, 2003). Online. Available: (www.ieee802.org/15/pub/2003/Mar03/02490r1P802-15_SG3a-Channel-Modeling-Subcommittee-Report-Final.zip).

[19] J.M. Cramer, R.A. Scholtz, and M.Z. Win, "On the Analysis of UWB Communication Channels," *in Proc. IEEE Conf. Military Commun.*, vol. 2, pp. 1191-1195, Oct. 1999.

[20] R.J.-M. Cramer, R.A. Scholtz, and M.Z. Win, "Evaluation of an Ultra-Wide-Band Propagation Channel," *IEEE Trans. Antennas Propagat.*, vol. 50, pp. 561-570, May 2002.

[21] J. Kunisch and J. Pamp, "Measurement Results and Modeling Aspects for the UWB Radio Channel," in *Proc. IEEE Conf. Ultra Wideband Systems and Technol.*, pp. 19-23, May 2002.

[22] J. Keignart and N. Daniele, "Subnanosecond UWB Channel Sounding in Frequency and Temporal Domain," in *Proc. IEEE Conf. Ultra Wideband Systems and Technol.*, pp. 25-30, May 2002.

[23] C. Prettie, D. Cheung, L. Rusch, and M. Ho, "Spatial Correlation of UWB Signals in a Home Environment," in *Proc. IEEE Conf. Ultra Wideband Systems and Technol.*, pp. 65-69, May 2002.

[24] W. Turin, R. Jana, S.S. Ghassemzadeh, C.W. Rice, and V. Tarokh, "Autoregressive Modeling of an Indoor UWB Channel," in *Proc. IEEE Conf. Ultra Wideband Systems and Technol.*, pp. 71-74, May 2002.

[25] S.S. Ghassemzadeh, L.J. Greenstein, A. Kavcic, T. Sveinsson, and V. Tarokh, "UWB Indoor Path Loss Model for Residential and Commercial Buildings," in *Proc. IEEE Conf. on Veh. Technol.*, vol. 5, pp. 3115-3119, Oct. 2003.

[26] S.S. Ghassemzadeh, L.J. Greenstein, A. Kavcic, T. Sveinsson, and V. Tarokh, "UWB Indoor Delay Profile Model for Residential and Commercial Environments," in *Proc. IEEE Conf. on Veh. Technol.*, vol. 5, pp. 3120-3125, Oct. 2003.

[27] S.S. Ghassemzadeh, L.J. Greenstein, T. Sveinsson, and V. Tarokh, "An Impulse Response Model for Residential Wireless Channels," in *Proc. IEEE Global Telecomm. Conf.*, vol. 3, pp. 1211-1215, Dec. 2003.

[28] S.S. Ghassemzadeh, L.J. Greenstein, A. Kavcic, T. Sveinsson, and V. Tarokh, "An Empirical Indoor Path Loss Model for Ultra-Wideband Channels," *J. of Commun. Networks* (Special Issue on Ultra-Wideband (UWB) Communications), vol. 5, no. 4, pp. 303-308, Dec. 2003.

[29] T.S. Rappaport, *Wireless Communications*: *Principles and Practice*, Prentice Hall, Reprinted July 1999, Chapters 3, 4, and 5.

[30] A.V. Oppenheim, R.W. Schafer, and J.R. Buck, *Discrete-Time Signal Processing*, Prentice Hall, second ed., 1999.

[31] V. Erceg, D.G. Michelson, S.S. Ghassemzadeh, L.J. Greenstein, A.J. Rustako, Jr., P.B. Guerlain, M.K. Dennison, R.S. Roman, D.J. Barnickel, S.C. Wang, and R.R. Miller, "A Model for the Multipath Delay Profile of Fixed Wireless Channels," *IEEE J. Select. Areas Commun.*, vol. 17, pp. 399-410, Mar. 1999.

[32] L.J. Greenstein, V. Erceg, Y.S. Yeh, and M.V. Clark, "A New Path-Gain/Delay-Spread Propagation Model for Digital Cellular Channels," *IEEE Trans. Veh. Technol.*, vol. 46, pp. 477-485, May 1997.